

Article

The Effect of Interfacial Roughness on Residual Stresses in Electron Beam-Physical Vapor Deposition of Thermal Barrier Coatings

Bochun Zhang ¹, Kuiying Chen ^{2,*} and Natalie Baddour ¹

¹ Department of Mechanical Engineering, the University of Ottawa, Ottawa, ON K1N 6N5, Canada; bzhan101@uottawa.ca (B.Z.); nbaddour@uottawa.ca (N.B.)

² Structures, Materials and Manufacturing Laboratory, Aerospace Research Centre, National Research Council Canada, Ottawa, ON K1N 6N5, Canada

* Correspondence: kuiying_chen@hotmail.ca or kuiying.chen@nrc-cnrc.gc.ca; Tel.: +1-613-993-1247; Fax: +1-613-949-8165

Abstract: Residual stresses play an essential role in determining the failure mechanisms and life of an electron beam-physical vapour deposition thermal barrier coating (EB-PVD TBC) system. In this paper, a new transitional roughness model was proposed and applied to describe the interfacial roughness profile during thermal cycles. Finite element models were implemented to calculate residual stresses at specific positions close to the interface of TBCs using temperature process-dependent model parameters. Combining stresses evaluated at valleys of the topcoat (TC) and excessive sharp tip roughness profiles, positions where the maximum out-of-plane residual stresses occur were identified and used to explain possible cracking routes of EB-PVD TBCs as interfacial roughness evolves during thermal cycling.

Keywords: stress model; FE model; temperature-process dependent parameters; evolution of interfacial roughness; parametric study; transitional roughness approximated model



Citation: Zhang, B.; Chen, K.; Baddour, N. The Effect of Interfacial Roughness on Residual Stresses in Electron Beam-Physical Vapor Deposition of Thermal Barrier Coatings. *Coatings* **2021**, *11*, 341. <https://doi.org/10.3390/coatings11030341>

Academic Editors: Daniel E. Mack and Narottam P. Bansal

Received: 25 January 2021

Accepted: 13 March 2021

Published: 17 March 2021

Publisher's Note: MDPI stays neutral with regard to jurisdictional claims in published maps and institutional affiliations.



Copyright: © 2021 by the authors. Licensee MDPI, Basel, Switzerland. This article is an open access article distributed under the terms and conditions of the Creative Commons Attribution (CC BY) license (<https://creativecommons.org/licenses/by/4.0/>).

1. Introduction

The residual stresses that develop close to the interface between layers play a significant role in determining the life span of an electron beam-physical vapor deposition (EB-PVD) thermal barrier coating (TBC) system. Many attempts have been made using analytical or numerical methods to estimate the stresses generated as a consequence of thermal expansion mismatch between layers and the growth of the thermally grown oxide (TGO) [1–7]. With additional factors taken into consideration and integrated into the stress model, calculated stresses and their distributions are expected to reflect the measured results, based on either isothermal or thermal cycling exposures. To date, process-dependent material properties have been shown to be significant in affecting the magnitude of stress levels, i.e., the variation of elastic modulus and coefficient of thermal expansion versus temperature, the change of strain rate-dependent creep or strain rate-independent yielding behaviour. Even a variation of phase components during progressive oxidation of the bond coat (BC) accompanying the swelling rate throughout the whole thickness of the TGO layer also greatly affects the stress levels during thermal cycles. A few analyses also focused on the pattern variation of interfacial roughness profiles, where typical roughness parameters were measured from the observed microstructures and used to characterize the roughness profiles versus temperature and exposure duration. The characterized roughness parameters from thermal cyclic experiments are used as input data in the current study [8]. The cross-sectional images of TBCs were provided at different stages of lifetime to illustrate the roughness variation under thermal cyclic experiments [9]. The effect of additional factors on the TBC durability, such as the TC (topcoat) fabrication method, the

high temperature, the cycle frequency and thermal gradient, were demonstrated with interaction of the interfacial roughness [10]. Different failure mechanisms of EB-PVD TBCs were developed based on the roughness level measured in the thermal cyclic experiments with the respective energy release rate (ERR) calculated [11]. The effects of a grit-blasting process on durability of EB-PVD TBCs are described [12]. However, less effort has been made on how a change in interfacial roughness affects the development of residual stresses [8–10], both of which could be critical in determining the possible positions where cracks nucleate at the maximum out-of-plane residual stresses estimated from the stress model. This, in turn, has a profound effect on determining the failure mechanisms of EB-PVD TBCs [11,12].

In this paper, the relationship between different roughness models and stress behaviour at critical positions where maximum stress levels could be obtained is analyzed. Finite element (FE) models are established by using the commercial finite element code ABAQUS. The method to characterize the roughness level of imperfections close to the interfaces is developed based on existing experimental data [13]. The material parameters of different layers are defined and integrated into the FE analysis. Parametric studies are conducted to examine the effect of geometrical parameters on the stress levels at specific positions within different layers including TC, TGO and bond coat (BC). A transitional model is proposed to illustrate the impact of global distance between imperfections on stress levels within imperfections. Possible failure modes of EB-PVD are further explained using both the variation of global interfacial roughness and the stress at a valley of the TC and ridge of the BC.

2. Compilation of Parameters and Integration into Finite Element (FE) Models Using Experimental Data under Thermal Cycles

In this section, the model parameters used for FE simulations are introduced. Two types of data were used; first, material properties for individual layers of TBC; second, geometrical parameters employed to illustrate the roughness profile at the interface between each layer extracted from experimental observations [13]. It is noted that these parameters are either temperature-dependent or temperature-process dependent, which indicates that material properties and roughness of interface vary as a function of temperature and time. Contrary to past studies that focused on a fixed roughness profile with constant geometrical parameters during geometrical sketching [1,7,14,15], a parametric study is conducted here, where varied geometrical roughness parameters are integrated into FE models to evaluate the effect of interfacial roughness on stress distributions. A set of geometrical parameters used in this parametric study are obtained from the failure time (177 h on 1151 °C), while the temperature process-dependent material properties are fully integrated into FE calculations. It is expected that a more comprehensive understanding based on the effect of interfacial roughness on stress distribution can be obtained by integrating these parameters into FE models.

2.1. Elastic Moduli and Coefficients of Thermal Expansion for Different Layers under the Cyclic Thermal Condition

The elastic moduli and coefficients of thermal expansion (CTE) for three different layers in EB-PVD TBCs are assumed to be temperature-process dependent and temperature-dependent, respectively. In high-temperature loading conditions, the effect of annealing treatment on the protective coating are considered to be significant in determining the coating materials properties which further affects the stress distribution throughout the thickness of coating layer [16]. It was experimentally found that the coating experiences a phase transformation and even crystallization process that would changes the material properties during the high-temperature annealing period [17]. This effect is also introduced in the current FE model where the elastic modulus of the TC is significantly affected by the sintering process during the isothermal exposure period, and also the modulus undergoes a drastic change during thermal cycles. For EB-PVD TBCs, the columnar structure of the TC with a large amount of external porosities between each column can be observed from scanning electron microscopy (SEM) cross-section images. At the same time, small internal

porosity and vertical segmentation cracks also exist within each column. According to a sintering study by Busso [1], it is assumed that for sintering of the EB-PVD TC, the elastic modulus of yttria-stabilized zirconia (YSZ) is only affected by the consolidation of internal porosities, while the external porosity remains unchanged throughout the high-temperature exposure. The effect of such consolidation and closure of internal pores on the elastic moduli of the transversely isotropic material E_{11} is shown in Figure 1, estimated at 1151 °C. For the coordinate system used in this study, all material properties for in-plane directions are represented by subscript 11 (x) and 33 (z), which are equivalent for most parameters, as illustrated in Figure 2. Thus, a 2D model is used, and transversely isotropic YSZ material properties are established.

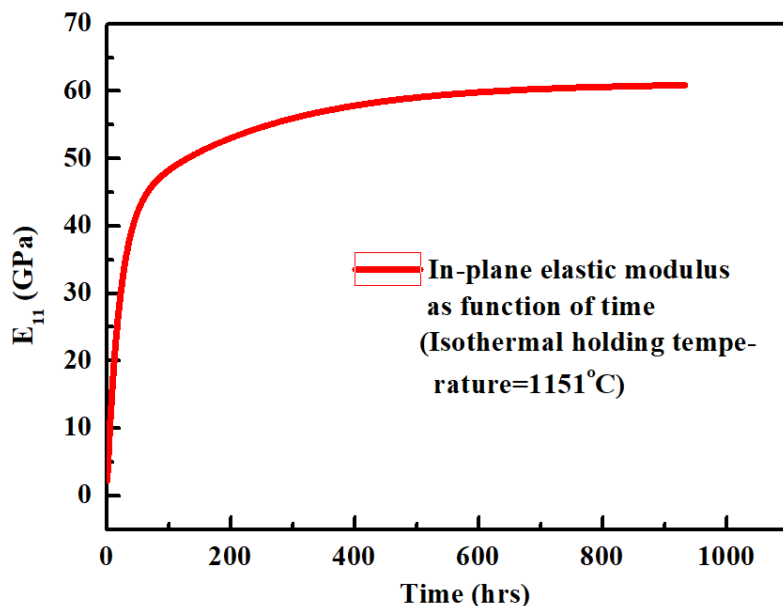


Figure 1. In-plane elastic modulus of topcoat (TC) in electron beam-physical vapor deposition thermal barrier coating (EB-PVD TBC) versus exposure time at 1151 °C, Equations (1) and (2) [1].

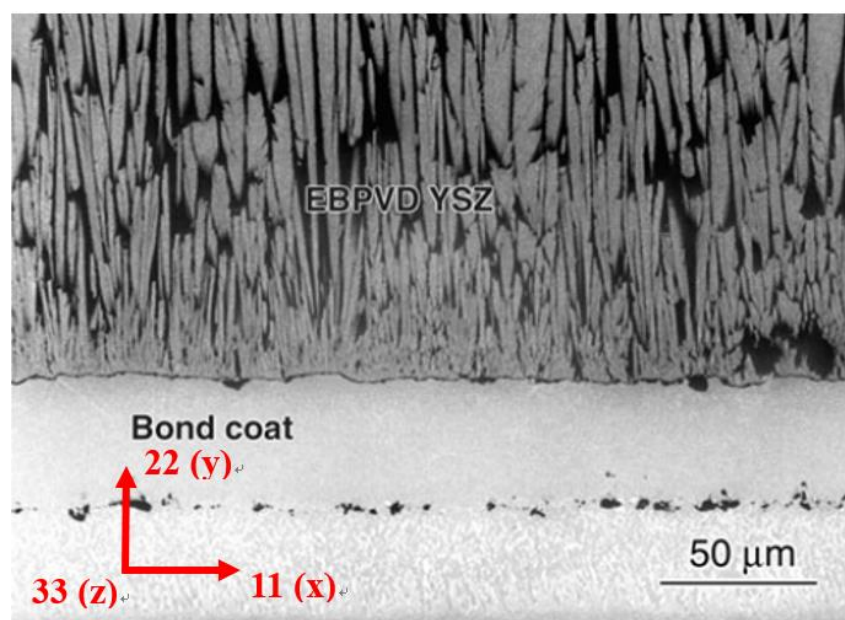


Figure 2. The red arrows indicate the local direction of the transversely isotropic axis of the ceramic top layer [18].

The sintering effect on the ceramic TC is represented by an increase in its time-dependent in-plane elastic modulus E_{11} given by,

$$E_{11}(t) = \left(\frac{\rho - \rho_0}{1 - \rho_0} \right) \times E_{22}(t) \quad (1)$$

$$\rho = 1 - (p_e + p_i) \quad (2)$$

where $E_{22}(t)$ is the time-dependent out-of-plane elastic modulus; ρ is the temperature-process-dependent total relative density of material; ρ_0 is the initial value of ρ before sintering. p_i and p_0 are the internal and external porosities of the YSZ TC.

For the anisotropic property of the TC layer, its time-dependent out-of-plane elastic modulus $E_{22}(t)$ is calculated by Equation (3), and the results are plotted versus thermal cycles in Figure 3,

$$E_{22}(t) = \left[1 + \frac{1.5(1 - \rho_i)(1 - v_{21})(9 + 5v_{21})}{7 - 5v_{21}} \right]^{-1} E_{22R} \quad (3)$$

where v_{21} is Poisson's ratio in the x-y direction, and E_{22R} is Young's modulus of fully dense isotropic zirconia.

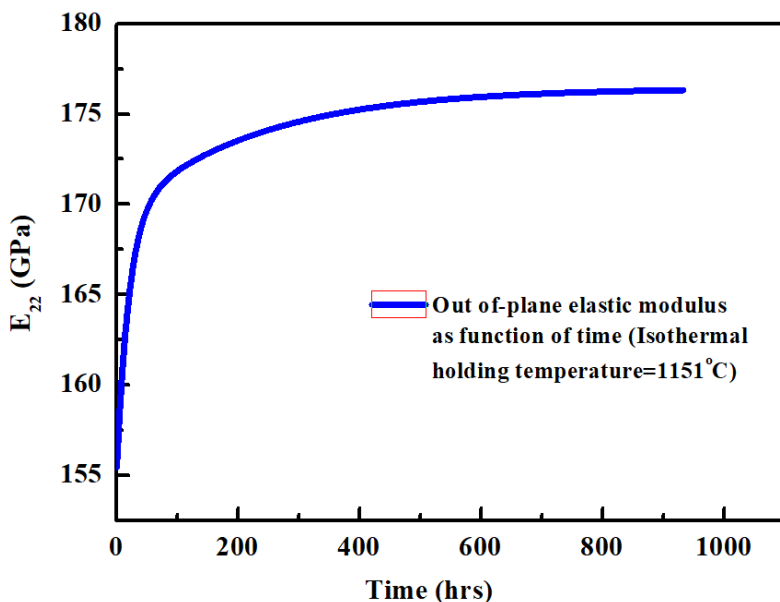


Figure 3. The out-of-plane elastic modulus $E_{22}(t)$ of TC in EB-PVD TBC versus exposure time, Equation (3).

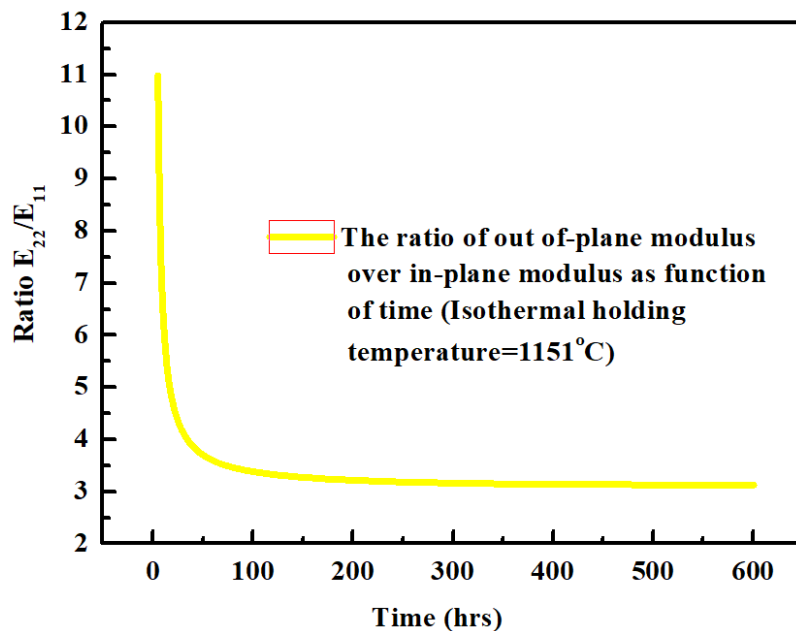
A ratio of the out-of-plane over the in-plane elastic moduli E_{22}/E_{11} is shown in Figure 4. The consolidation and closure of pores within the columnar structures due to the sintering effect result in a considerable increase of in-plane elastic-modulus compared to out-of-plane elastic modulus. This explains the drop in the ratio of these two elastic moduli.

Table 1 shows elastic moduli E_{11} and E_{22} versus temperature after sintering for 100 h at 1151 °C [7].

It is difficult to measure the variation of elastic modulus during thermal cycles. To simulate temperature-dependent elastic modulus under thermal cycling, it is assumed that the increase in elastic modulus as temperature drops follows the same pattern as the decrease as temperature increases. Within a thermal cycle dwell duration, the elastic modulus is affected mainly by sintering; during the heating and cooling processes, the sintering effect can be ignored.

Table 1. The elastic moduli variation versus temperature [7].

T (K)	293	473	773	973	1173	1373	1473
E_{11} (Gpa)	67	64	61	59	58	56	56
E_{22} (Gpa)	205	196	188	182	178	174	173

**Figure 4.** The ratio of out-of-plane elastic modulus to in-plane modulus versus exposure time.

In order to model the pattern of elastic modulus variation versus temperature, the elastic moduli from Table 1 are approximated by,

$$E_{22}(T) = \gamma_2 \exp\left(\frac{\zeta_2}{T + \omega_2}\right) + E_{20}(t) \quad (4)$$

$$E_{11}(T) = \gamma_1 \exp\left(\frac{\zeta_1}{T + \omega_1}\right) + E_{10}(t) \quad (5)$$

where γ_i , ζ_i and ω_i are fitting parameters. $E_{i0}(t)$ are also time-dependent moduli of the TC during the dwell period within a cycle calculated at the end of the previous thermal cycle by Equations (1) and (3).

The cyclic temperature profile ($^{\circ}\text{C}$) for heating ($0 < t < t_1$), dwell duration ($t_1 < t < t_2$), and cooling period ($t_2 < t < t_3$) can be described by:

$$T(t) = \begin{cases} 112.6 \times t + 20 & (0 \leq t < t_1) \\ 1151 & (t_1 \leq t < t_2) \\ -112.6 \times t + 6761 & (t_2 \leq t < t_3) \end{cases} \quad (6)$$

In Equation (6), t_i ($i = 1, 2, 3$) denotes the different moments during the history of thermal cycling, i.e., the heating time, holding dwell time and cooling time, respectively. The cyclic behavior of the in-plane and out-of-plane elastic moduli can be obtained by combining the time-dependent elastic modulus calculated from Equations (1)–(3) as well as temperature-dependent elastic modulus calculated by substituting Equation (6) into Equations (4) and (5). The temperature fluctuation, as well as the variation of in-plane and out-of-plane elastic moduli within 300 min, are shown in Figures 5–7.

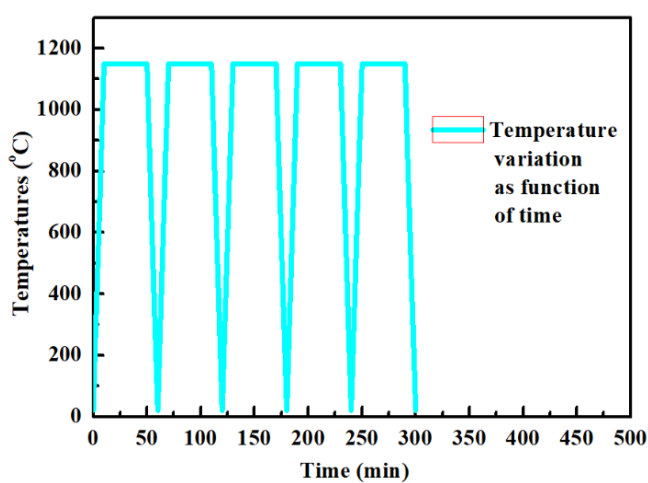


Figure 5. Temperature variation used in finite element (FE) simulation under cyclic thermal conditions, Equation (6) [13].

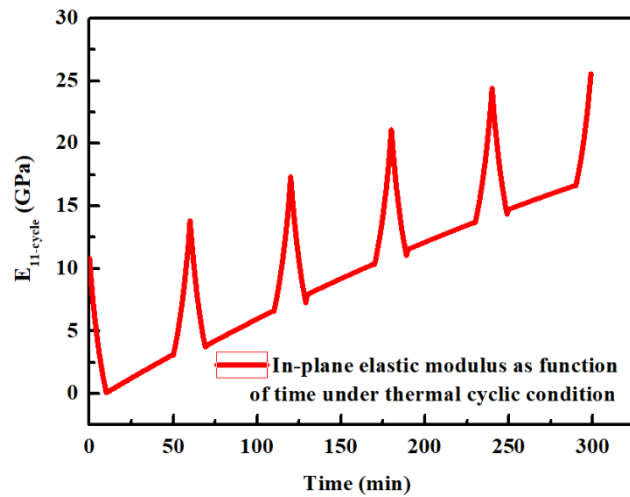


Figure 6. In-plane elastic modulus as a function of time under cyclic thermal conditions, Equations (1), (2), (5) and (6).

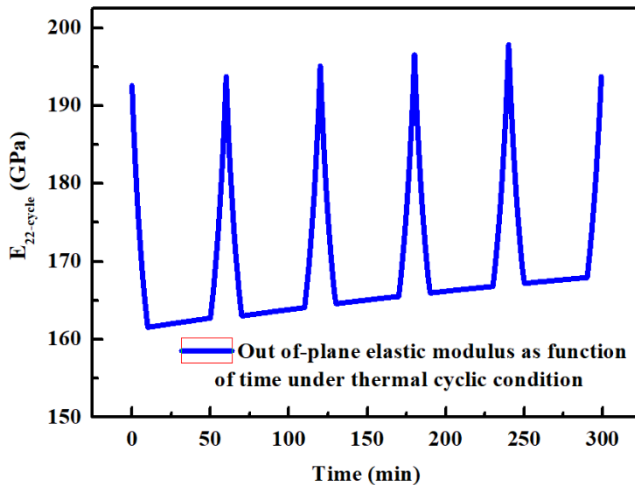


Figure 7. Out-of-plane elastic modulus as a function of time under cyclic thermal conditions, Equations (3), (5) and (6).

Moreover, the in- and out-of-plane elastic modulus of the TC for full lifetime at 1151 °C is depicted in Figure 8.

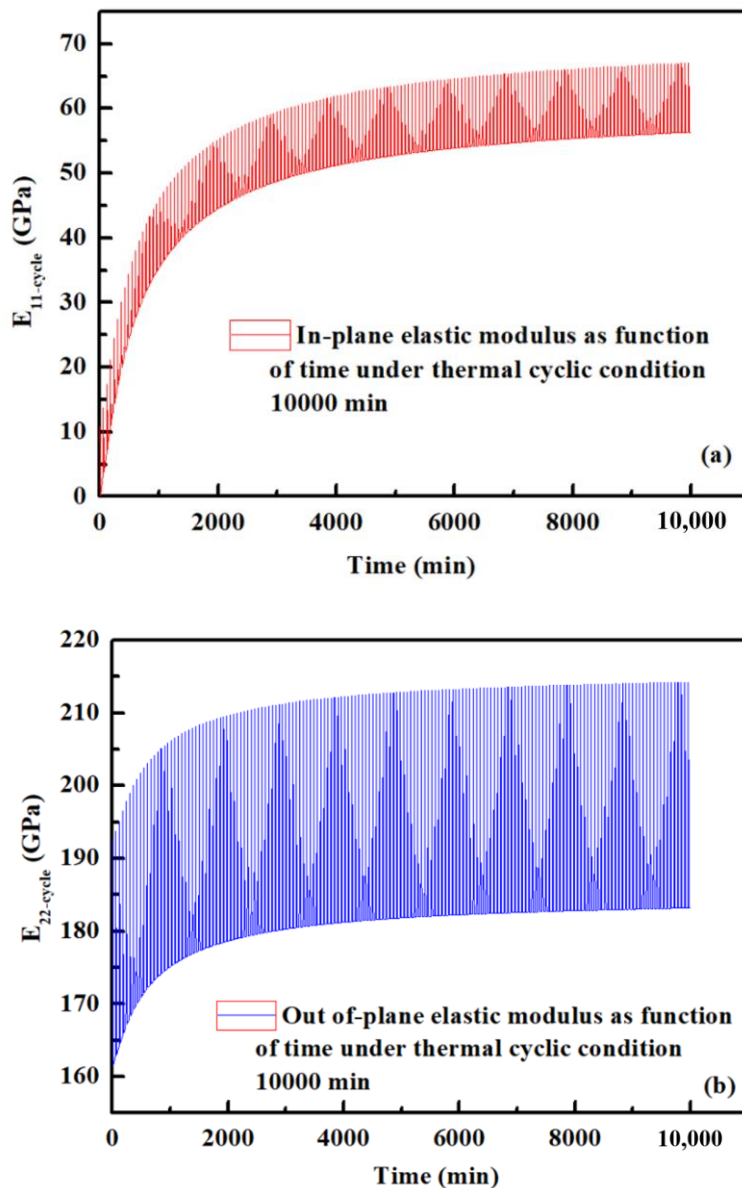


Figure 8. The general trend for elastic modulus as a function of time under cyclic thermal condition (10,000 min) (a) in-plane Equations (1), (2), (5) and (6) (b) out-of-plane Equations (3), (5) and (6).

In contrast to the TC, there is no sintering effect on the elastic moduli of both TGO and BC layers; their elastic moduli $E_{BC}(T)$ and $E_{TGO}(T)$ are temperature-dependent only [7], as given by:

$$E_{TGO}(T) = -0.07506 \times T + 448 \text{ (Gpa)} \quad (7)$$

$$E_{BC}(T) = -0.02329 \times T + 123.9 \text{ (Gpa)} \quad (8)$$

The temperature dependence of their coefficient of thermal expansion are [7] given by:

$$\alpha_{TBC}(T) = (0.0003636 \times T + 9.615) \times 10^{-6} \quad (9)$$

$$\alpha_{TGO}(T) = (0.001388 \times T + 7.532) \times 10^{-6} \quad (10)$$

$$\alpha_{BC}(T) = (0.005021 \times T + 10.83) \times 10^{-6} \quad (11)$$

where $\alpha_{TBC}(T)$, $\alpha_{TGO}(T)$ and $\alpha_{BC}(T)$ represent the temperature-dependent coefficients of thermal expansion for the TC, TGO and BC, respectively.

2.2. Creep, Swelling and Inelastic Behaviour of the Bond Coat/Thermally Grown Oxide (BC/TGO) Layers

The inelastic behaviour of BC/TGO layers is described by creep formulae [7], which are incorporated into the FE calculations. The creep strain rate of the BC is evaluated in terms of the equivalent von Mises stress σ^V , elastic modulus E_{BC} and temperature T , Equation (12). For the creep formulae of the TGO, no elastic modulus of TGO is involved in the creep rate evaluation. These two creep rates are represented by,

$$\dot{\varepsilon}_{BC}^{cr} = 6.3 \times 10^{13} \left(\frac{\sigma_{BC}^V}{E_{BC}} \right)^4 \exp\left(-\frac{125,000}{8.314T}\right) \quad (12)$$

$$\dot{\varepsilon}_{TGO}^{cr} = 6.8 \times 10^3 \left(\sigma_{TGO}^V \right)^{2.3} \exp\left(-\frac{424,000}{8.314T}\right) \quad (13)$$

Specifically, Equation (12) is used to describe the creep property for Pt-NiAl BC, while Equation (13) is used to describe the creep behaviour of alpha-alumina TGO. Both of those materials are modelled as being isotropic and homogeneous.

The inelastic behaviour describing the strain rate generated due to oxidation from the Pt-NiAl BC to alpha-alumina TGO is taken from Busso et al. [14] as:

$$\dot{\varepsilon}_{TGO}^{SW} = f_2^{ini} \dot{f}_{(Ni,Pt)Al} \left(\sqrt{\frac{3}{2}} P \frac{T'}{S} + e_V^T 1 \right) \quad (14)$$

where the inelastic stretching tensor $\dot{\varepsilon}_{TGO}^{SW}$ represents the non-recoverable deformation rate induced by oxidation of the metallic phase, f_2^{ini} is the initial volume fraction of metallic phase, which has not been oxidized, $f_2^{ini} = 0.38$ according to [7]. P is a coefficient depending on the shape of the oxide particles. S and T' are the norm and deviatoric components of the aggregate stress tensor, respectively. e_V^T is the mean local dilatational strain induced by the transformation of the initial metallic phase. $\dot{f}_{(Ni,Pt)Al}$ indicates the evolution of the internal variable $f_{(Ni,Pt)Al}$, which is defined as the normalized fraction of the oxidizing phase which has chemically reacted with O_2 , varying in a value from 0, before the oxidation begins, to 1 when primary oxidation is completed. Parabolic formulae are used to describe the TGO growth from the Pt-NiAl BC oxidation. The internal variables $f_{(Ni,Pt)Al}$ are defined as:

$$f_{(Ni,Pt)Al} = \frac{A_{TGO} e^{-\frac{Q_{TGO}}{k_B T}} t^{p_{TGO}}}{d_{TGO}^{tot}} \quad (15)$$

where d_{TGO}^{tot} is the total thickness of the oxidized layer within a specific life span. A_{TGO} , Q_{TGO} and p_{TGO} are the coefficient of TGO growth rate, TGO growth activation energy and TGO growth exponent, respectively. Further, t is an exposure holding duration and k_B is the Boltzmann constant. It is noted [14] that Equation (15) is only valid when the local oxygen concentration $C_O > C_{0Cr}$, where C_O is oxygen concentration and C_{0Cr} is the critical oxygen concentration which defines the onset of oxidation. In addition, it is noted that the TGO growth strains do not develop isotropically, i.e., the normal and parallel strains due to BC oxidation to form TGO behave differently, their ratio is taken as approximately 87 [1] and was applied into the current FE model.

The temperature-dependent yield strengths of both BC and TGO [15,19] shown in Figures 9 and 10, are incorporated into the FE calculations. For the current study, the inelastic behaviour of both BC and TGO layers is partially determined by their strain rate-independent yield strengths. Specifically, when the creep rates are very small at

low temperatures, the relative large CTE mismatch strain is accommodated by inelastic deformation, which is likely to be controlled by rate independent plasticity.

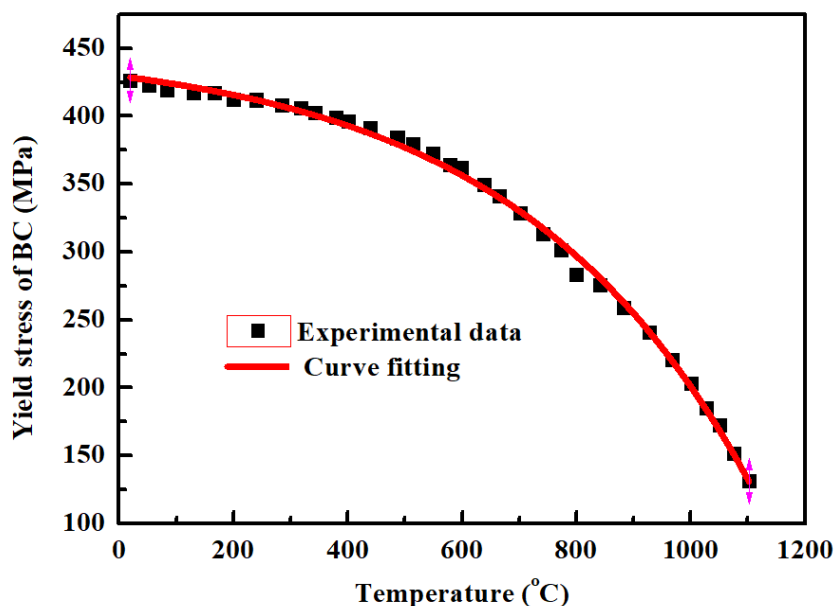


Figure 9. The rate-independent yield stress of bond coat (BC) reported by Cheng et al. [15] at different temperatures together with the fitting curve.

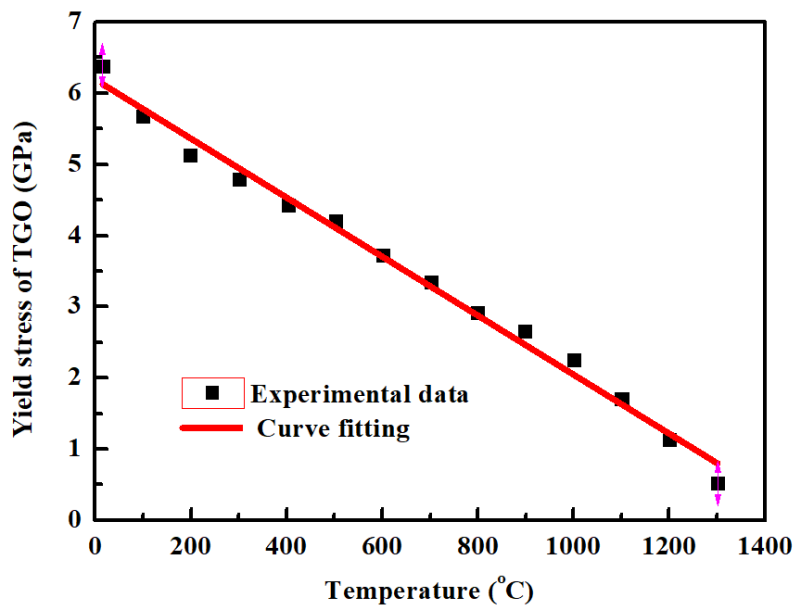


Figure 10. The rate-independent yield stress of thermally grown oxide (TGO) reported by Sánchez-González et al. together with the fitting curve.

2.3. Temperature-Process Dependent Geometrical Parameters

According to Wen et al. [13], the geometrical parameters used to characterize the interfacial roughness profile vary as a function of thermal cycles. It is reasonable to assume that different stress levels will be obtained by the inclusion of different roughness profiles into the FE model, where those roughness profiles are characterized by geometrical parameters measured at different stages of cyclic thermal experiments.

A key feature of our model is the assumption of similarity in the roughness profile between the TC/TGO interface and TGO/BC interface since the thickness of the TGO layer

is relatively small compared to the entire TBC. This approximation avoids duplicating the measurement and characterization of roughness parameters at the TC/TGO interface for different thermal cycles. For previous analytical and numerical models, the local roughness of the BC surface was mostly characterized by using amplitude and horizontal length of localized imperfections (so-called wavelength) for both atmospheric plasma-sprayed thermal barrier coating systems (APS-TBCs) [10,20–22] and EB-PVD TBCs [2,11–13]. However, the method to evaluate the roughness profile for EB-PVD TBCs should be significantly different from that of APS-TBCs [13]. Hence, a new method to characterize the local roughness of BC surface for EB-PVD is proposed in this section.

Contrary to APS-TBCs where time-independent interfacial roughness parameters are used, the evolution of interfacial roughness in EB-PVD TBCs is significant as the thermal cycle proceeds. Several methods have been proposed to characterize the variation of interfacial roughness as a function of both temperature and thermal cycles, such as the RMS (root mean square) and tortuosity (L/L_0). L and L_0 for tortuosity are defined as the length of a surface roughness curve and the measured linear distance from beginning to end of the specific defined interfacial roughness profile at a specific number of cycles, respectively [13]. The interfacial roughness profiles for bond-coated-only and YSZ-coated interfaces were measured experimentally [13]. As mentioned in the previous section, a set of geometrical parameters used for the parametric study are obtained from the interfacial roughness profile at the failure stage of a life cycle. Specifically, using the parameters (a) amplitude of interfacial roughness; (b) width of interfacial roughness; combined with (c) TGO thickness, the geometry of the interfacial roughness between TGO/BC can be fully described. Subsequently, (d) positions where residual stresses are calculated are chosen. Each of the parameters (a) to (d) are discussed below.

2.3.1. Amplitude

It is obvious that experimentally determined amplitude and tortuosity of interfacial roughness vary as the thermal cycle proceeds [13]. This variation of interfacial roughness is temperature-process dependent, which is different from APS-TBCs. The amplitude of interfacial roughness A is expressed as the root mean square of roughness parameter (RMS) by:

$$A = \sqrt{2}RMS \quad (16)$$

The resulting mean amplitude is plotted in Figure 11.

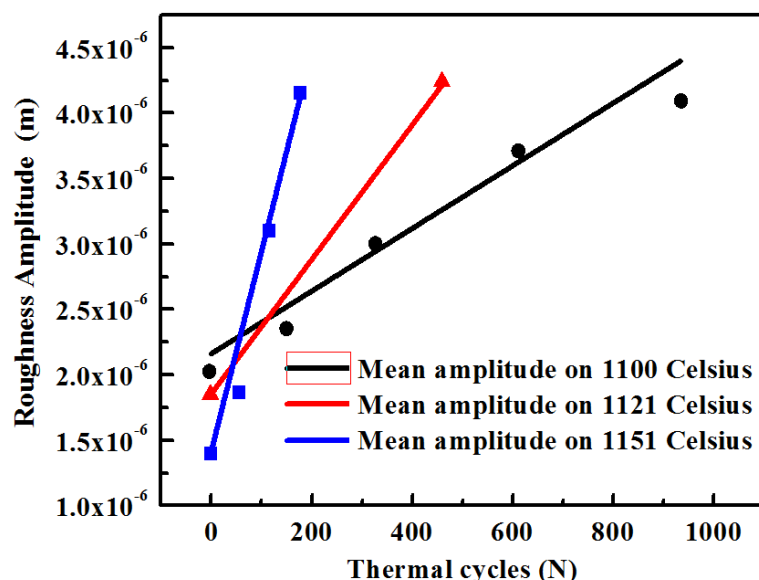


Figure 11. Mean amplitude of roughness with respect to thermal cycles at different temperatures, Equation (16) [13].

2.3.2. Width

A specific method to characterize the horizontal width of the interfacial roughness is necessary in order to evaluate the stress in EB-PVD TBCs. Consider the tortuosity of the interfacial roughness; the physical implication behind it can be understood as the ratio of the length of a rough surface over a defined flat surface. The random distribution of roughness is reflected by irregular heights over each individual protuberance. This can be treated as a uniformly distributed rumpling profile either in the form of an isosceles triangle or ellipse, Figure 12. Considering the triangular-roughness approximation, the hypotenuse of the triangle in each uniform roughness profile is given by $L/L_0 \times W/2$, where $W/2$ is the half-length of the bottom side, Figure 13.

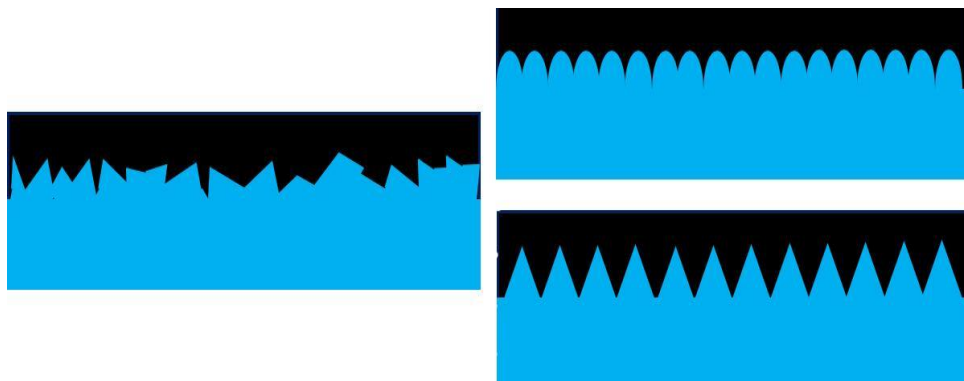


Figure 12. Two ways of equivalent simulated roughness profile according to scanning electron microscope (SEM) images.

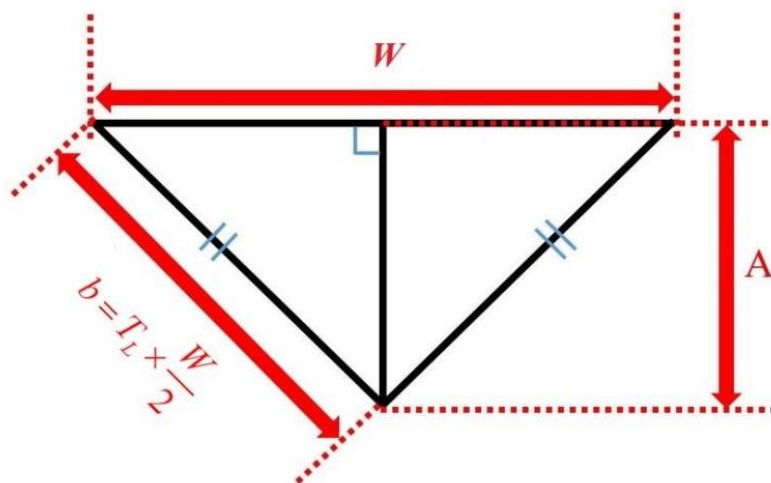


Figure 13. Schematic diagram of interfacial roughness profile approximated in the form of a triangle.

It is assumed that an individual interfacial roughness curve with a flat base forms an isosceles triangle, Figure 13. The horizontal width of the interfacial roughness can be represented by the length of the base W . The total length of two hypotenuses, indicating the length of each uniform roughness profile, is described via the product of tortuosity and width $T_L \times W$, which increases as a function of temperature. The height of an isosceles triangle is represented by an average amplitude of roughness A . Therefore, the length of the hypotenuse b , as well as the length of the base, W can be determined by combining the amplitude (height) and the tortuosity (the ratio of the length of two hypotenuses over the base-side) as:

$$b = T_L \times \frac{W}{2} \quad (17)$$

$$W = \frac{2 \times A}{\sqrt{T_L^2 - 1}} \quad (18)$$

where T_L is tortuosity as defined in [13], $T_L = L/L_0$. The resulting width of roughness, which is defined as W , can be obtained by integrating tortuosity and amplitude as functions of the number of cycles and temperature, Figure 14.

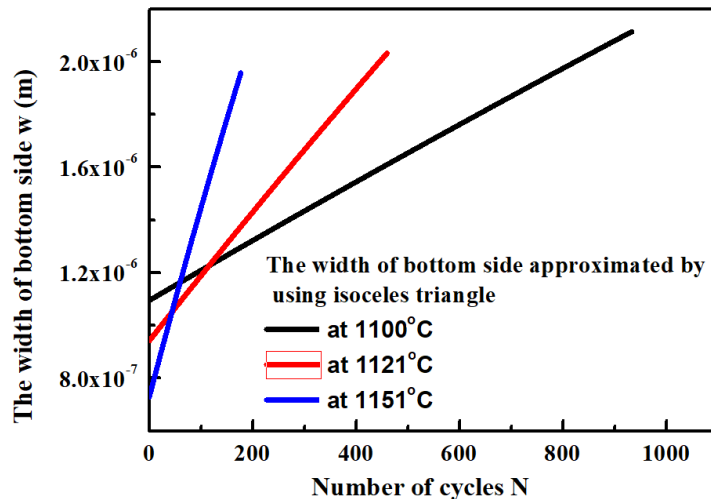


Figure 14. The width of the bottom-side approximated by an isosceles triangle as a function of thermal cycles and temperature, Equation (18).

2.3.3. TGO Thickness

As a by-product of progressive oxidation of the BC, the thickness of the TGO between TC and BC has a large effect on the stress distribution within TBCs. The thickness of TGO scale was measured during thermal cycling in [13] at 1151 °C. In this paper, the TGO growth model is fitted to these measured data and described using a parabolic law as

$$d_{TGO} = A_{TGO} e^{-\frac{Q_{TGO}}{k_B T} t} P_{TGO} \quad (19)$$

where A_{TGO} , Q_{TGO} and P_{TGO} are the same as in Equation (15). The fitting curve, together with experimentally measured TGO thickness, is shown in Figure 15.

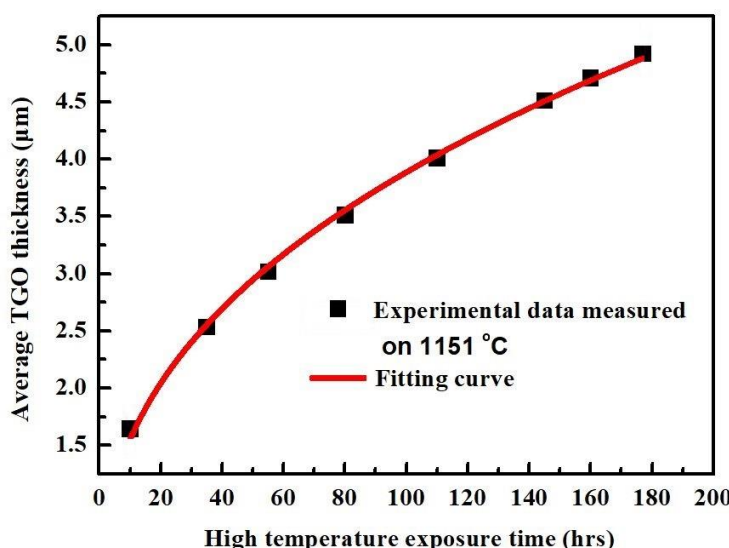


Figure 15. The average TGO thickness versus exposure time at 1151 °C, Equation (19) [13].

2.3.4. Positions for Residual Stress Evaluations

Compared to prior work that focused on specific positions close to the interface where only the maximum residual stress was identified [22], the current work calculates residual stresses as a function of position. Therefore, by examining different locations in the FE analysis, it is possible to find the maximum stress level at which the crack nucleates. Meanwhile, the relationship between the resulting stress and position is established, which, in turn, provides valuable information for establishing analytical stress models. The relative distance between the TC/TGO interface to the positions (y) are shown in Figure 16, at which the stresses will be evaluated specifically.

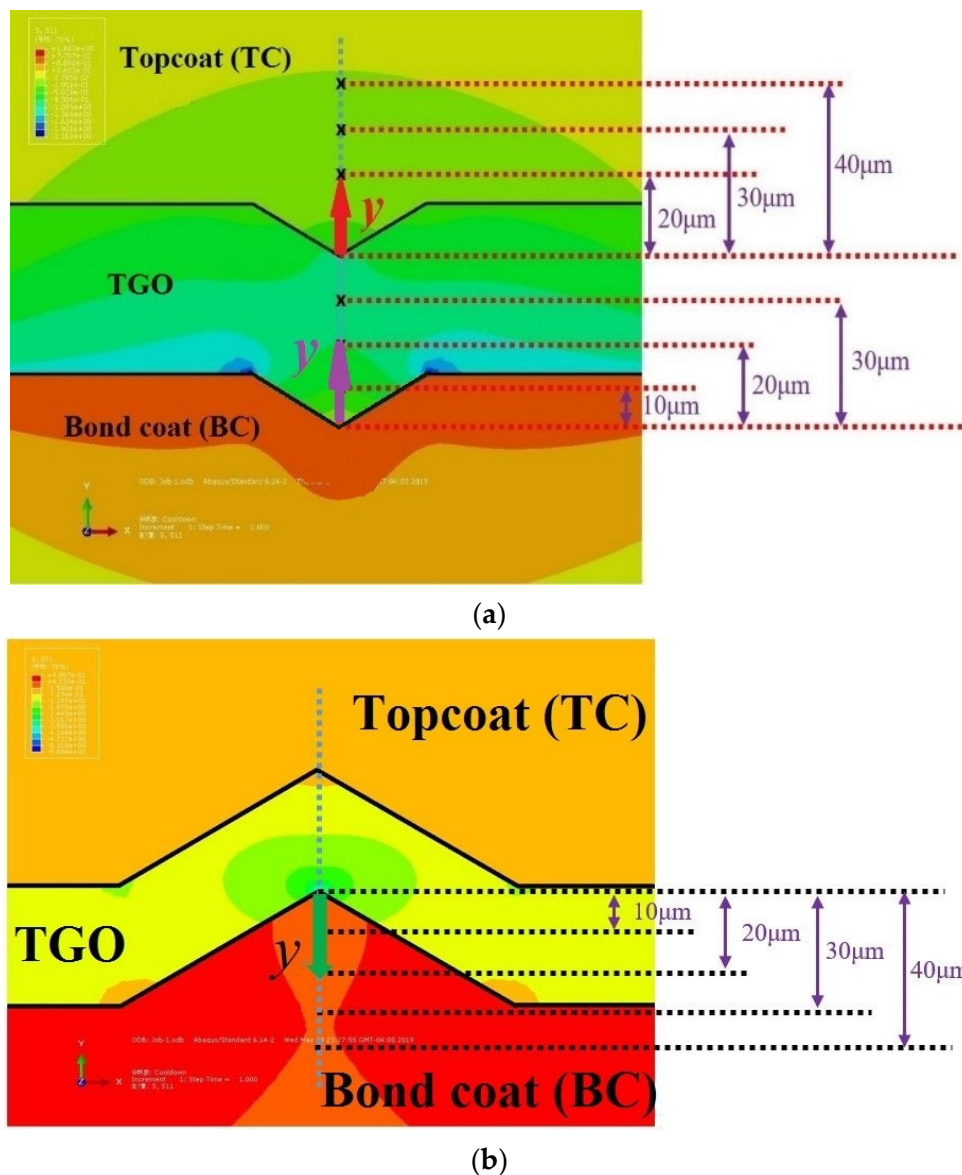


Figure 16. The schematic diagram of positions where stresses are calculated, (a) the stresses within the TC and TGO layer, (b) the stresses within the BC layer.

3. Finite Element (FE) Model

3.1. Thermal Barrier Coating (TBC) Morphology

The goal of FE modelling in this work is to determine the effect of roughness profile on stress levels. The temperature-process dependent model parameters are incorporated into FE calculations. The typical geometrical parameters applied to modelling layers of the TBC system are obtained using Equations (16), (18) and (19) at failure time during thermal

cycling. After a close inspection of representative sections of the TGO–ceramic interface, its morphology was idealized as a periodic array of saw-type segments, as indicated by Figure 12. The corresponding periodic unit cell in the FE model is shown in Figure 17, and details about interfacial morphology are examined closely in Figure 18.

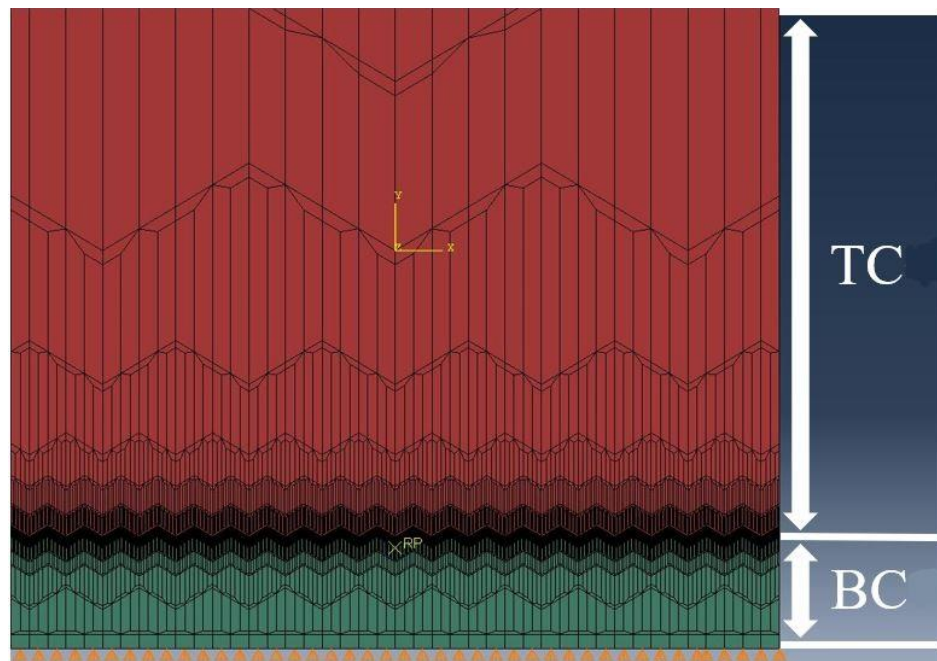


Figure 17. Typical FE mesh used in the TBC model for a BC surface roughness at a ratio $A/W \approx 0.5992$.

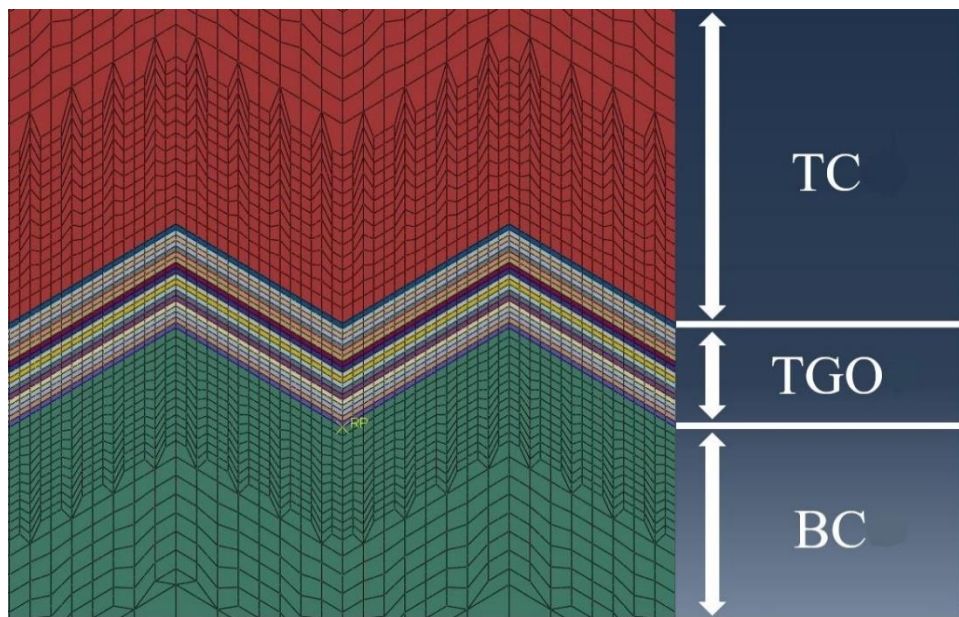


Figure 18. Details of the interfacial morphology simulated at 177 cycles from cyclic thermal experiments; the roughness profile is characterized in the form of triangles.

Here, the amplitude of the interface, denoted A in Figure 13, is approximately $4.12 \mu\text{m}$, and the length of the bottom side, denoted, W is approximately $13.76 \mu\text{m}$. Thus, interface morphologies with $A/W \simeq 0.3$ aspect ratios will be used at the failure cycle (177 h under 1151°C). The FE meshes consist of 39,572 quadratic generalized plane strain elements with full integration.

3.2. Transversely Isotropic Yttria-Stabilized Zirconia (YSZ) Materials for Topcoat (TC)

For simplification, the current 2D model is established where the thickness of TBC in the z-direction is not considered in the current stress analysis, since the elastic strain is only defined in the 2D cross-sectional plane. The transversely isotropic elastic properties of materials are applied to the general plane strain cross-section defined for a TC layer since it is anisotropic between the in-plane and out-of-plane directions. Thus, the resulting fourth-order elastic compliance tensor, S , becomes:

$$S = \begin{bmatrix} 1/E_1 & -v_{21}/E_2 & -v_{13}/E_1 & 0 & 0 & 0 \\ -v_{12}/E_1 & 1/E_2 & -v_{12}/E_1 & 0 & 0 & 0 \\ -v_{13}/E_1 & -v_{21}/E_2 & 1/E_1 & 0 & 0 & 0 \\ 0 & 0 & 0 & 1/G_2 & 0 & 0 \\ 0 & 0 & 0 & 0 & 1/G_1 & 0 \\ 0 & 0 & 0 & 0 & 0 & 1/G_2 \end{bmatrix} \quad (20)$$

According to the designation of the axes from the coordinate system, Figure 2, v_{21} and v_{12} are defined as Poisson's ratio in the x-y direction, and v_{13} is the in-plane Poisson's ratio in the x-z direction. v_{23} is Poisson's ratio in the y-z direction, which is equivalent to v_{21} based on the application of orthotropic elasticity within the TC layer. The shear moduli with the same subscripts are also defined, that is G_{12} and G_{23} represent the shear moduli in the x-y and y-z directions, respectively, where G_{13} is defined as the in-plane shear modulus in the x-z direction.

The definition of orthotropic elasticity by specifying the engineering constants, the relative elastic modulus, shear modulus as well as Poisson's ratio in terms of different directions of TC materials are given in Table 2, where x, y, z in the FE calculation indicate the directions of 1, 2, 3, respectively.

Table 2. The definition of orthotropic elasticity by specifying the engineering constants.

Parameters	Definition	Conversion to Transversely Isotropic Elastic Properties
E_{11}	In-plane elastic modulus in the x-direction	E_{11} estimated by Equations (1) and (5).
E_{22}	Out-of-plane elastic modulus in the y-direction	E_{22} estimated by Equations (3) and (4)
E_{33}	Out-of-plane elastic modulus in the z-direction	$E_{33} = E_{11}$
v_{12}	Poisson's ratio in the x-y direction	$v_{21} = 0.2, v_{12} = v_{21} \times \frac{E_{11}}{E_{22}}$
v_{13}	In-plane Poisson's ratio	$v_{13} = 0.12$ [7]
v_{23}	Poisson's ratio in y-z direction	$v_{21} = v_{23} = 0.2$
G_{12}	Shear modulus in the x-y direction	$G_{12} = G_2 = E_{22}/E_{11} \times G_1$
G_{13}	In-plane Shear modulus	$G_{13} = G_1 = E_{11}/2(1 + v_{13})$
G_{23}	Shear modulus in the y-z direction	$G_{23} = G_2 = E_{22}/E_{11} \times G_1$

The temperature in TBC was assumed to be spatially homogeneous and to vary cyclically with time, as illustrated in Figure 5. The peak cycle temperature of 1151 °C was identified as a typical TBC metal/ceramic interface temperature. The residual stresses will be calculated only at a temperature below 20 °C. In addition, the TBCs are considered to be stress-free (or with a small compressive state) during the high temperature dwell period at 1151 °C, where the stress is relaxed by the creep deformation according to Equations (12) and (13). The surface of the TBC is assumed to be traction free and symmet-

ric, and periodic boundary conditions are assumed on the bottom plane of the BC $y = 0$, indicating no vertical downward movement through the y-direction due to support by the BC/substrate layer.

3.3. Phase Transformation and Oxidation Model

There are two effects to consider when simulating the oxidation from metallic BC to oxide (TGO), as this process involves a gradual change of mechanical properties and creep effects from the BC to the TGO, and initiation of the swelling effect since TGO starts to form. In this study, it is assumed that the progressive oxidation is dominated by internal oxidation, in which a new oxide layer forms at the interface between the BC and existing TGO layer. The FE model starts with two layers, i.e., the TC and BC.

To implement a progressive oxidation of the metallic BC to form oxide TGO in FE models, the maximum thickness of TGO, d_{\max}^{tot} , was initially selected at the failure cycle of TBCs at specific exposure temperatures from testing samples. This transitional layer d_{\max}^{tot} was then used to simulate TGO formation in FE models. According to this scheme, the initial BC thickness d_{BC}^{int} is partitioned into two regions, i.e., d_{BC}^{tot} and d_{BC}^{rev} , and follows $d_{BC}^{int} = d_{BC}^{tot} + d_{BC}^{rev}$, where the thickness d_{BC}^{rev} is never oxidized during the entire thermal exposure period, and $d_{BC}^{tot} \ll d_{BC}^{int}$. Before the BC starts oxidation, the entire d_{BC}^{int} behaves as pure metallic properties. As BC oxidation proceeds, a portion d_{OX}^i of the BC is converted into the TGO scale progressively. Therefore, the oxide fraction within this d_{BC}^{tot} region is $f_{(Ni,Pt)Al} = d_{OX}^i / d_{BC}^{tot}$. It is assumed that the mechanical properties for this transition d_{BC}^{tot} layer can be estimated from mechanical properties BC and TGO by

$$E_{tr} = E_{TGO} \times f_{(Ni,Pt)Al} + E_{BC} \times (1 - f_{(Ni,Pt)Al}) \quad (21)$$

where the definitions of E_{BC} , E_{TGO} and $f_{(Ni,Pt)Al}$ can be found in preceding sections. Equation (21) describes the mechanical properties of the “TGO” layer that undergoes phase transformation. Similarly, the temperature dependence of the coefficient of thermal expansion and inelastic creep strain rate for the TGO layer can be estimated from:

$$\alpha_{tr} = \alpha_{TGO} \times f_{(Ni,Pt)Al} + \alpha_{BC} \times (1 - f_{(Ni,Pt)Al}) \quad (22)$$

$$\dot{\varepsilon}_{tr}^{cr} = \dot{\varepsilon}_{TGO}^{cr} \times f_{(Ni,Pt)Al} + \dot{\varepsilon}_{BC}^{cr} \times (1 - f_{(Ni,Pt)Al}) \quad (23)$$

To implement TGO swelling during the phase transformation process, it is necessary to obtain the time to initiate the phase transformation from the top to the bottom of the TGO layer. However, it is obvious that the TGO growth rate decreases as oxidation occurs at deeper positions, Figure 15. This is because the formation of the relatively dense alpha-alumina as a newly formed TGO layer, to some degree, prevents the BC surface from further oxidation. Accordingly, in order to integrate the effect of gradually-decreased oxidizing rate from the surface to the bottom of a pre-defined TGO layer, several sublayers are further partitioned with an identical thickness within the TGO section, as shown in Figure 18. Obviously, it takes longer for oxidation completion at the sublayer close to the bottom of the TGO compared to that near the surface of the TGO. Thus, for each sublayer within the TGO, the time for oxidation completion can be derived by rewriting Equation (19) as

$$t_n^F = \left(\frac{n \times d_{TGO}^{sub}}{A_{TGO} e^{-\frac{E_{TGO}}{k_B T}}} \right)^{\frac{1}{P_{TGO}}} \quad (24)$$

Here, t_n^F is the time for oxidation completion for each sublayer, where n indicates the number of sublayers counting from top to bottom, d_{TGO}^{sub} is the thickness of the sublayer, which is defined according to the total number of sublayers within the TGO section.

To achieve the desired TGO thickness versus oxidation history for each sublayer, the coefficient of TGO growth rate A_{TGO} needs to be re-calculated using Equations (19) and (24) as

$$A_{TGOi} = \begin{cases} \frac{d_{TGO}^{sub}}{e^{-\frac{Q_{TGO}}{\kappa_B T}} (t_i^F)^{P_{TGO}}} & \text{for } n = 1 \\ \frac{d_{TGO}^{sub}}{e^{-\frac{Q_{TGO}}{\kappa_B T}} (t_i^F - t_{i-1}^F)^{P_{TGO}}} & \text{for } n > 1 \end{cases} \quad (25)$$

where A_{TGOi} is the coefficient of the TGO growth rate for sublayer i ($i = 1$ to n) within the TGO section. Accordingly, the evolution of the internal variable $f_{(Ni,Pt)Al}$ for each sublayer can be rewritten as,

$$f_{(Ni,Pt)Al-i} = \begin{cases} \frac{A_{TGOi} e^{-\frac{Q_{TGO}}{\kappa_B T}} t_i^{P_{TGO}}}{d_{TGO}^{sub}} & \text{for } n = 1 \\ \frac{A_{TGOi} e^{-\frac{Q_{TGO}}{\kappa_B T}} (t_i^F - t_{i-1}^F)^{P_{TGO}}}{d_{TGO}^{sub}} & \text{for } n > 1 \end{cases} \quad (26)$$

$$f_{(Ni,Pt)Al-i} = \begin{cases} 0 & \text{if } f_{(Ni,Pt)Al-i} \leq 0 \\ 1 & \text{if } f_{(Ni,Pt)Al-i} \geq 1 \end{cases}$$

where $f_{(Ni,Pt)Al-i}$ is the evolution of the internal variable for each sublayer. Subsequently, the mechanical, thermal properties and creep behaviour of the sublayers can be obtained by substituting Equation (26) into Equations (21)–(23). The FE model of EB-PVD TBCs can now be defined based on the previously described constitutive material models. These are implemented numerically as a user-defined subroutine in commercial FE code ABAQUS [23].

4. Results and Discussion

4.1. Parametric Study of the Effect of Local Geometrical Parameters on Stress Distribution of TBC

The magnitude of residual stress at a valley of the TBC/TGO interface is governed by not only temperature-dependent material properties such as sintering of the TC and inelastic behaviour of the TGO and BC, but also by the interface roughness between each layer [10,24,25] characterized using temperature-process dependent localized geometrical parameters. To analyze the effect of those parameters on residual stresses, a parametric study is conducted where an isosceles triangle is used to approximate the interfacial roughness profile. Three parameters are incorporated into the FE model: (i) A is amplitude and indicates the height of a triangle, (ii) W is the width and indicates the length of the bottom side of triangle applied to defining the shape of triangular imperfection, and (iii) the position y is used to describe the locations $(y_{TC}, y_{TGO}, y_{BC})$ where the stresses are evaluated, Figure 19.

To characterize the effect of each parameter on stress, a parametric study using the controlled variants is applied to the FE analysis (FEA). At position y , residual stresses are calculated while allowing variations of amplitude A and width W . Also, for a given amplitude A and width W , stresses are calculated at various positions y . A reference set of parameters used to characterize the roughness profile are selected from experimental results at the failure cycle of 177 h of TBC exposed at 1151 °C. The geometrical parameters used in the FEA model are presented in Table 3.

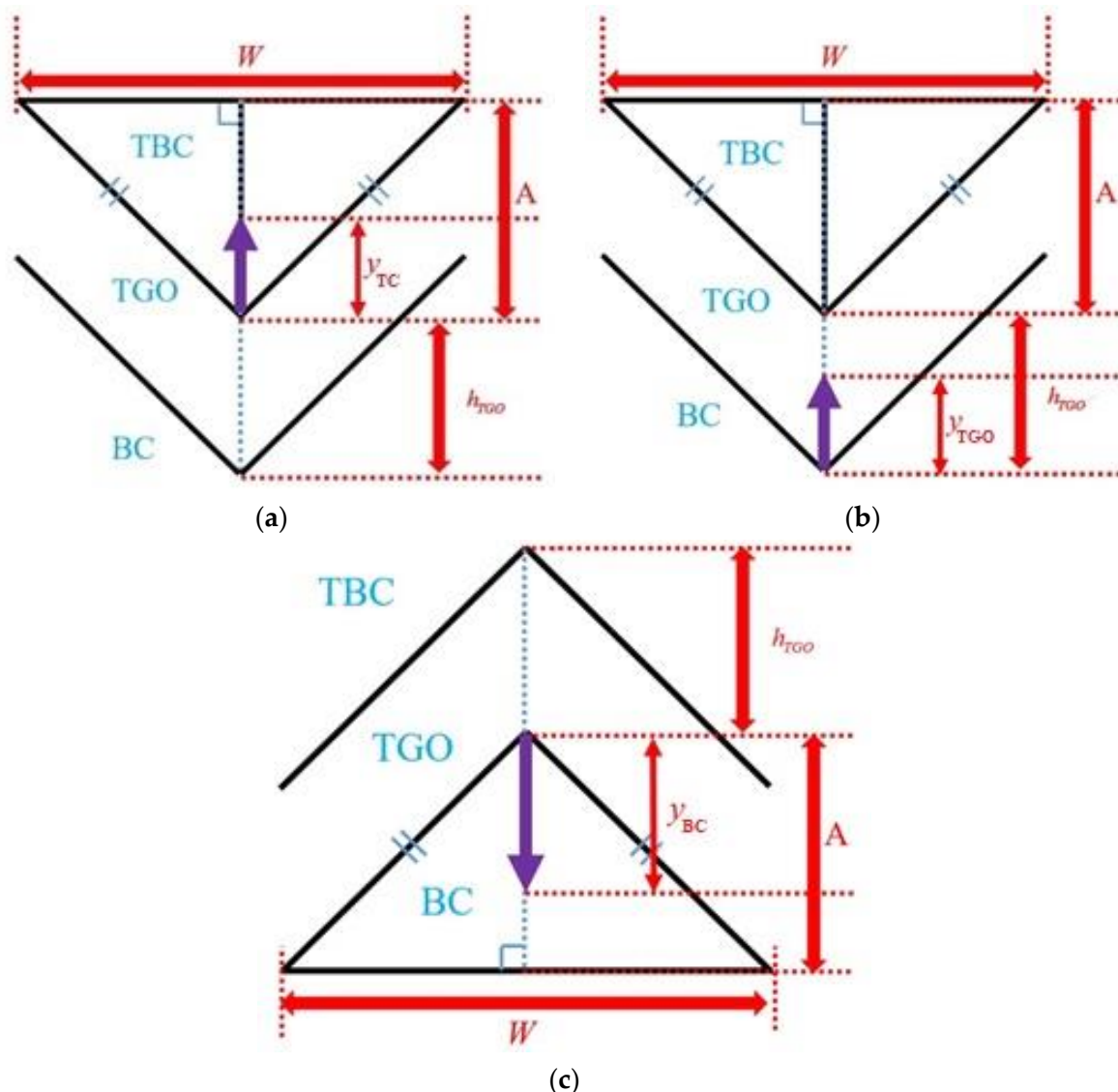


Figure 19. Schematic diagram of individual interfacial roughness profile used for a parametric study where amplitude, width, TGO thickness as well as positions are illustrated for different layers. (a) TC layer, (b) TGO layer, and (c) BC layer.

Table 3. Reference set of roughness parameters used in the FE model at $N = 177$ h at 1151 $^{\circ}$ C [13].

Properties	Value	Unit
Amplitude A	4.12	μm
Width W	13.76	μm
Total TGO thickness d_{TGO}	4.92	μm
Relative position y_{TC} or y_{BC}	1.27 (TC) or 0.43 (BC)	μm

4.1.1. The Effect of Roughness Amplitude on Stress at the Valley of TC and Ridge of BC

The effect of roughness amplitude on residual stress is analyzed for both the TC and BC layer. In addition to the amplitude A for the reference group, $0.5 A$ and $1.5 A$ of the amplitudes are also used for FE calculations. The resulting stresses, together with those from the reference group, are used to assess a correlation of out-of-plane residual stresses versus amplitude. The models depicting the geometric roughness are presented in Figure 20.

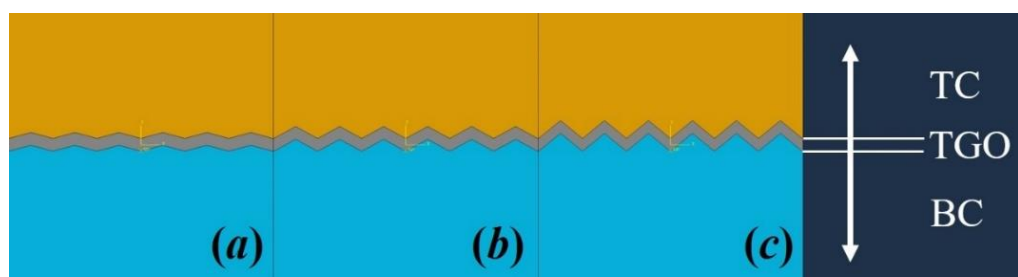


Figure 20. Amplitude variation of (a) $0.5\text{ }\mu\text{m}$, (b) A and (c) $1.5\text{ }\mu\text{m}$ listed from left to right where the rest of the parameters are kept constant.

The stresses from the valley of the TC are calculated and plotted in Figure 21 as a function of time.

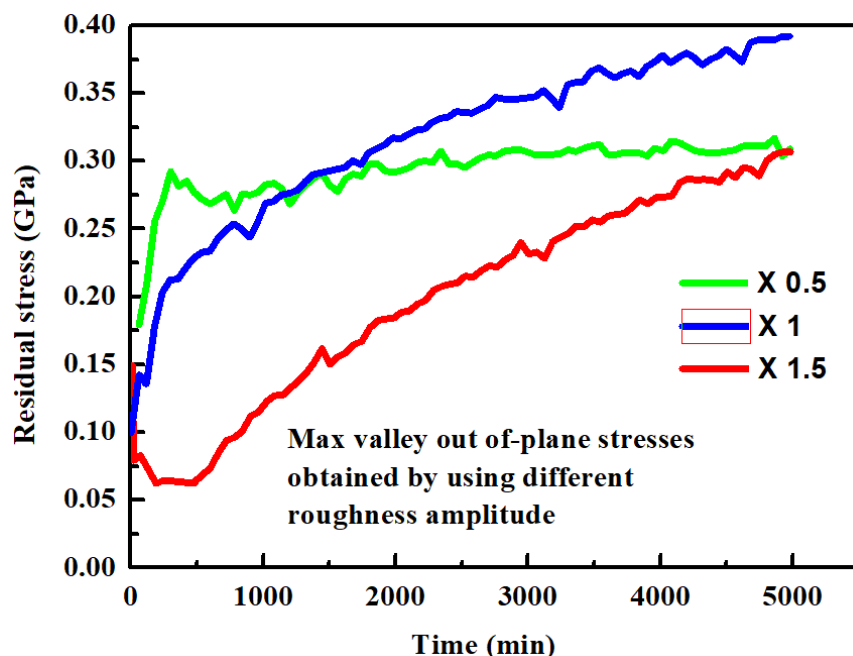


Figure 21. Out-of-plane residual stresses at the valley of TC with different roughness amplitude as thermal cycle proceeds.

It was suggested in [7] that increasing the amplitude of imperfection roughness would increase the stress close to the interface, since the stress concentration is boosted by increasing sharpness at the tip of roughness. However, the red curve in Figure 21 shows an opposite effect on stresses in a large roughness amplitude. Because the positions with respect to the interface are identical for these three cases in the FE model, the deeper the amplitude used in interfacial roughness mapping, the narrower the tip at the valley of the TC. It seems that there is a prohibitive effect on the stress estimated at the tip of the TC as the sharpness of the geometrical roughness reaches a critical value. This is reflected by a lower stress obtained from the valley of the TC when $1.5\text{ }\mu\text{m}$ amplitude is used in the FE model. For the stress obtained from the peak of the BC, the effect of different amplitudes exerts a profound effect on stress level according to the FE results, as can be seen in Figure 22.

It is observed that most of the roughness develops during the rumpling of the BC as a consequence of creep during high-temperature exposure. The creep proceeds to accommodate large mismatch stress during a fast heating period. The amplitude of the roughness of the BC surface is directly affected by the rumpling kinetics, resulting in a further increase of stress and delamination crack nucleation at the TGO/BC interface.

However, for the stresses distributed within the TC, according to the failure analysis in [4,17], it is at the middle stage of thermal cycling that delamination cracks are generated by coalescence of voids located at the valley of the TC. This may indicate that as the thermal cycle proceeds, the increase of roughness amplitude facilitates the development of out-of-plane residual stress at the valley of the TC, while the out-of-plane stress developed at the early stage of thermal cycles with initial large roughness amplitude is not large enough to initiate crack nucleation. This avoids early crack generation within the TC layer.

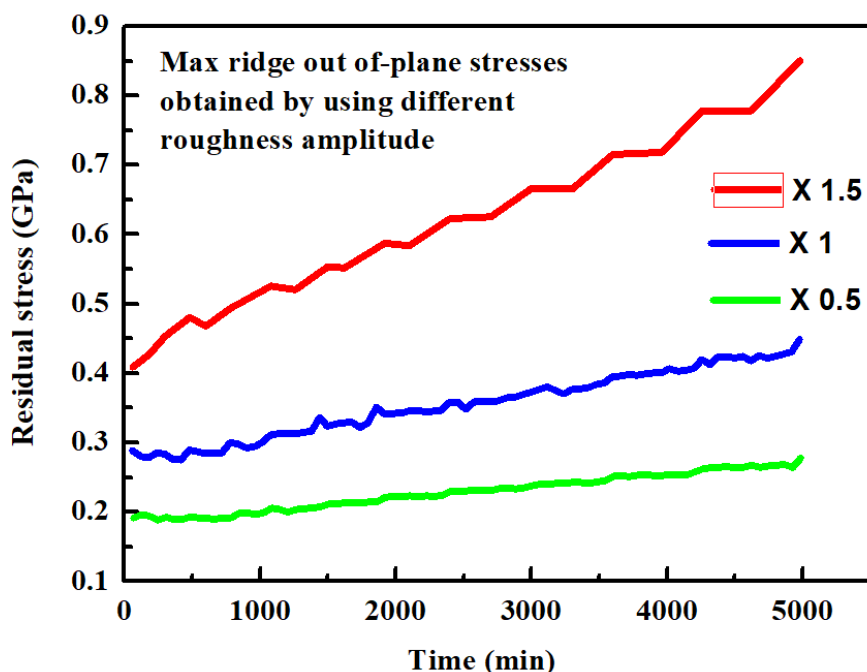


Figure 22. Out-of-plane residual stresses at peak of BC with different roughness amplitudes as thermal cycle proceeds.

4.1.2. Effect of Roughness Width on Stress at the Valley of TC and Ridge of BC

Similar to the analysis in the preceding section, the effect of roughness width W on residual stress is analyzed for both TC and BC layers. In addition to the width W from the reference group, two other cases of 0.5 W and 1.5 W widths were studied. The models depicting the geometric roughness are presented in Figure 23.

The stresses at the valley of the TC versus exposure duration are plotted in Figure 24.

Based on Figure 24, it appears that the narrowing width W has a similar effect as increasing the amplitude A on stress distributions. That is, higher stresses are expected for rougher interfacial roughness, characterized either by a higher amplitude (the blue curve in Figure 21) or by a narrower width at the middle stage of thermal cycles (the green curve in Figure 24). However, it should be noted that with an invariant width of the overall TBC FE model, the amount of roughness varies as a function of the individual width of imperfections, Figure 23. It is obvious that more imperfections will be incorporated into FE calculations as the width of individual imperfections is assumed to be narrower. Although there is a rapid growth in residual stress calculated from narrower roughness profiles (the green curve in Figure 24), a lower stress state is obtained initially. This phenomenon can be explained in two ways. On the one hand, the narrower roughness profiles boost the stress concentration at the valley of the TC, which in turn raises the stress on individual imperfections; this can be seen for the calculated stresses at the peak of the BC, Figure 25. On the other hand, the intensive interaction between relatively close neighbouring imperfections impedes the development of out-of-plane tensile stresses within the TC.

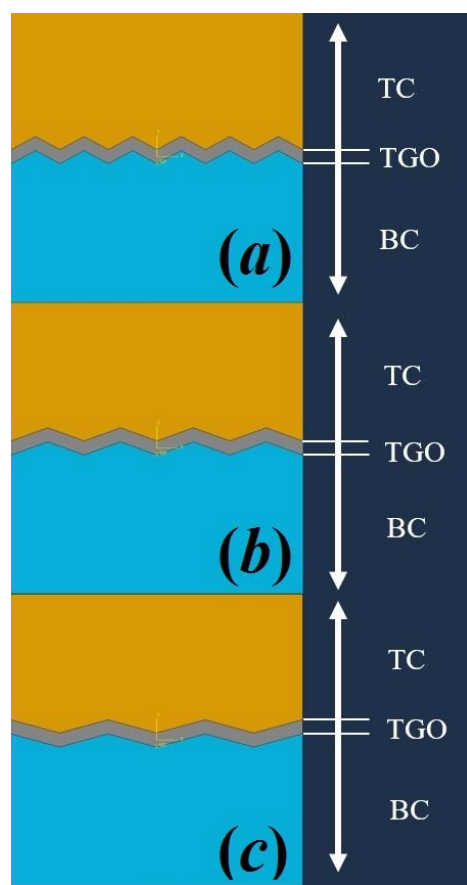


Figure 23. Width variation of (a) 0.5 W (b) W and (c) 1.5 W listed from top to bottom where the remaining parameters are kept constant.

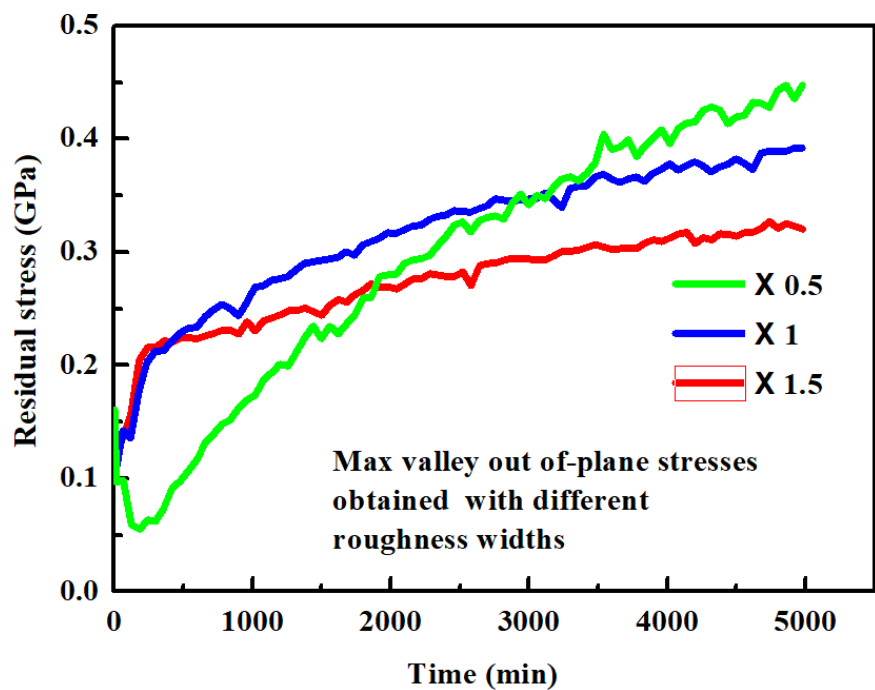


Figure 24. Out-of-plane residual stresses at the valley of the TC with different roughness width versus thermal cycle.

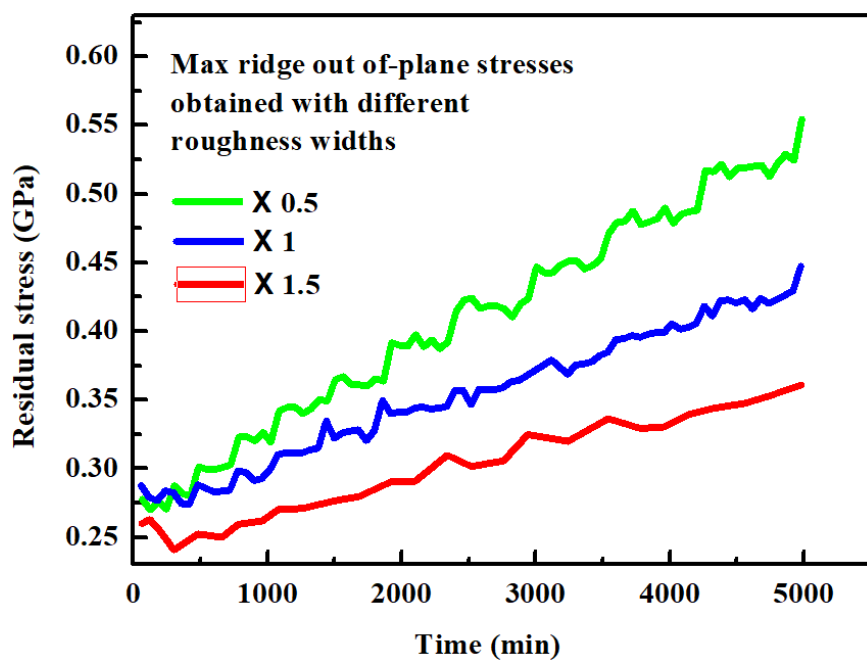


Figure 25. Out-of-plane residual stress at the peak of BC with different roughness width as thermal cycle proceeds.

4.1.3. Correlation between Positions and Stresses at the Valley of TC and Ridge of BC

The residual stresses were calculated under different amplitudes and widths. Meanwhile, the calculated stresses are different at selected positions at the bottom of the TC and ridge of the BC. Five relative positions with different “ y ” in Figure 16 are selected at the valley of the TC and ridge of the BC close to the interface, where a total of 10 residual stresses are calculated, respectively. The geometry of interfacial roughness is characterized using roughness parameters measured at 177 cycles based on amplitude and width experimental data, Table 3. The maximum out-of-plane cooling stresses calculated at different positions away from the valley of the TC are plotted versus time in Figure 26, with different y_{TC} as shown in Figure 19a.

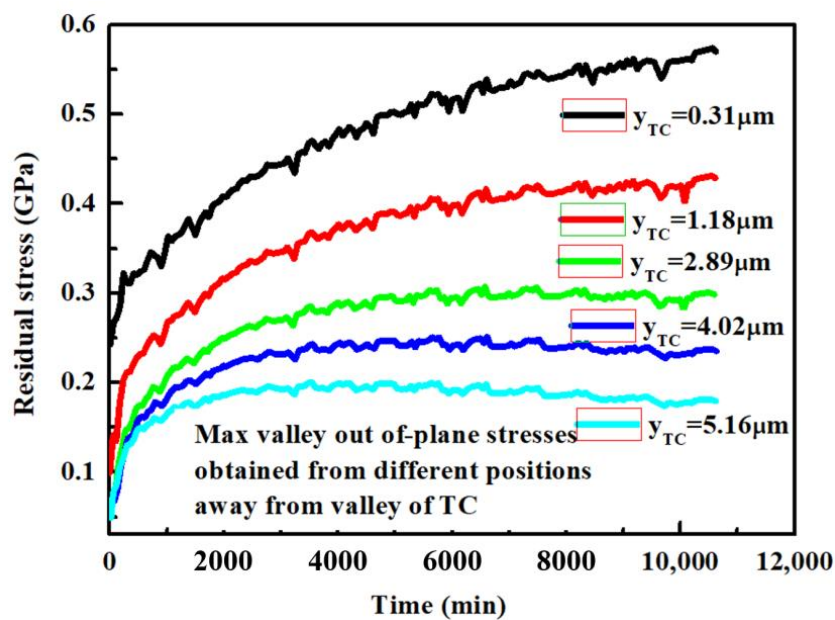


Figure 26. Out-of-plane tensile stresses calculated at the valley of the TC as a function of time at various positions.

It is expected that a higher level of stresses close to the interface is due to larger strains from either coefficient of thermal expansion mismatch (CTE mismatch) between different layers or volumetric expansion due to oxidation of the BC layer. It can also be seen that stresses away from the interface increase uniformly compared to those close to the interface. Concerning the complexity of multi-layers in TBC, there exists a relatively large fluctuation of residual stresses close to the interface within the TC. Moreover, it should be mentioned that residual stresses are calculated for the roughness profile with an amplitude equal to $4.12\text{ }\mu\text{m}$. The cyan curve of stresses illustrated in Figure 26 is at the position of $5.16\text{ }\mu\text{m}$ away from the valley of the BC, a position that is located outside of the valley of TC. The general trend of all curves, including the cyan curve, suggests that the out-of-plane residual stress decreases when moving away from the valley of the TC.

It can be expected that the possible region of cracks where the maximum out-of-plane stress occurs is close to the interface within the valley of the TC. However, it was observed that the positions where the maximum stress occurs are shifted away from the bottom of the TC valley, as previously mentioned. This is possible for some interfacial roughness observed from the experimental cross-sectional area; for example, the interfacial roughness with a very sharp tip where the ratio of amplitude over width exceeds a critical value.

The higher maximum out-of-plane cooling stress is also obtained close to the interface at the ridge of the BC, as seen in Figure 27 with different y_{BC} as shown in Figure 19c. Similar to the residual stresses at the valley of the TC, there is a high possibility for crack nucleation at the peak of the BC close to the interface where the highest out-of-plane residual stress occurs.

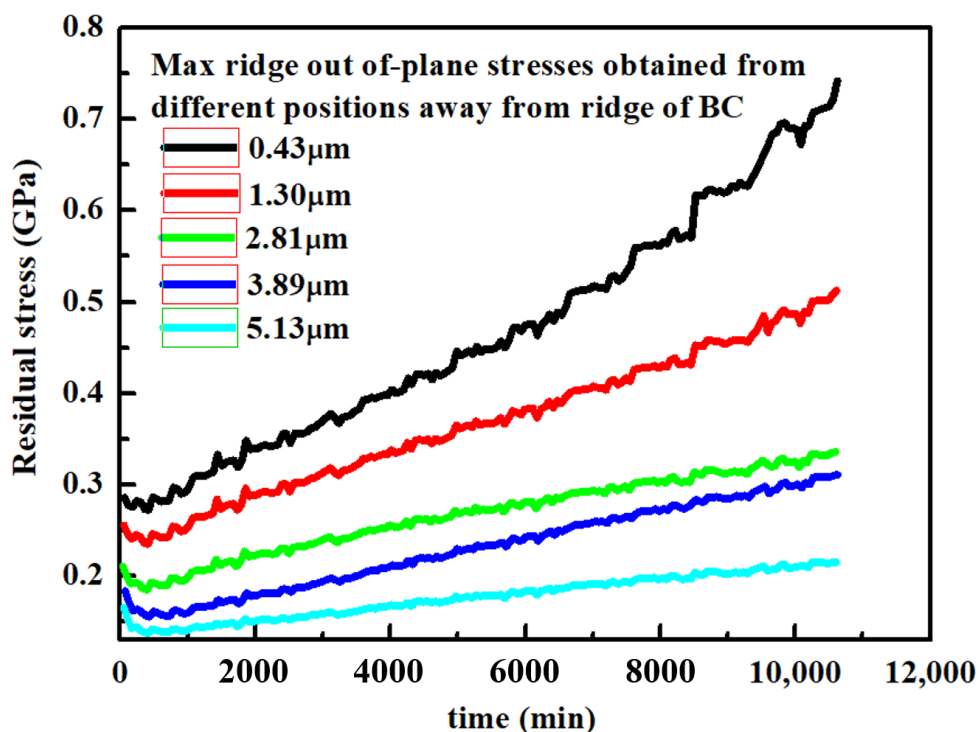


Figure 27. Out-of-plane tensile stresses calculated at the ridge of the BC as a function of time at selected positions.

4.2. Generalized Imperfection Model and the Impact of Distance between Imperfections on Stress Distributions

One of the geometrical parameters used to model the roughness profile, the width of the bottom side of the imperfection, is derived using experimentally measured tortuosity.

According to the schematic diagram of triangular approximated roughness in Figure 13, the tortuosity can be expressed as,

$$T_L = \frac{2 \times b}{W} \quad (27)$$

For a single imperfection described in the form of a triangle, the larger the tortuosity, the sharper the angle of the valley. As can be seen in Figure 28, for those two triangular-shaped imperfections, assuming the amplitudes are identical ($A = A'$), the imperfection shown in Figure 28b has higher tortuosity than that in Figure 28a ($T_{L'} > T_L$). According to Equation (18), the one with higher tortuosity has a narrower width, which is shown for a single imperfection model in Figure 28.

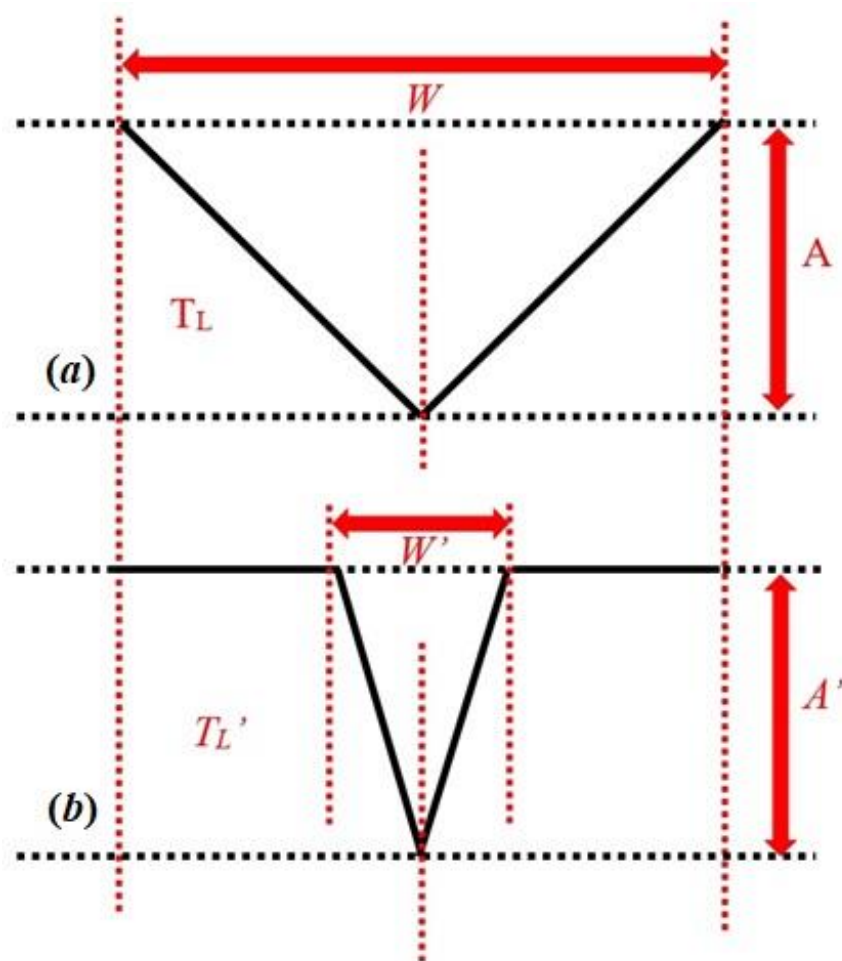


Figure 28. Schematic diagram describing the relationship between tortuosity and width of interfacial roughness imperfection for a single imperfection. The interface roughness profile with (a) lower tortuosity and wider width, (b) higher tortuosity and narrower width.

However, for multiple imperfections closely located at the interface, it becomes more complicated to estimate the tortuosity for a defined length of the roughness profile. As can be seen in Figure 29, it is still assumed that the amplitudes are identical for triangular approximated imperfection ($A = A'$). This indicates that the tortuosity is higher for the individual “narrower” imperfection in Figure 29b than the “wider” one in Figure 29a. However, this discrepancy can be supplemented by adding additional “wider” imperfections within a defined length. The tortuosity for two sets of connected imperfections, according to Figure 29, might be identical ($T_{L'} \simeq T_L$).

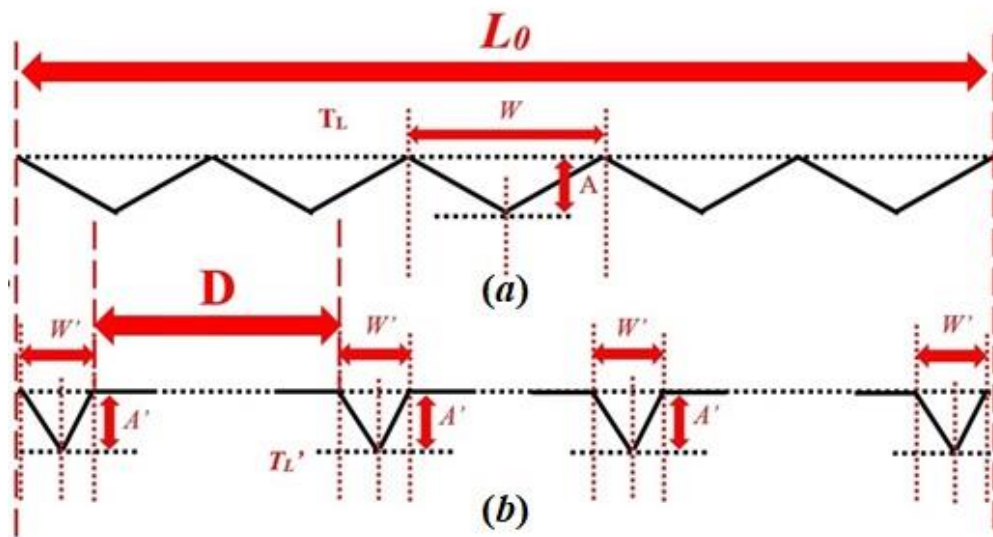


Figure 29. Schematic diagram describing the relationship between tortuosity and width of interfacial roughness imperfection for multiple imperfections. The total tortuosity might be identical for both of interfacial roughness profile characterized by (a) lower individual tortuosity with wider width, (b) higher individual tortuosity with narrower width.

However, it is obvious that the width of an individual imperfection is not the same in the roughness profile of Figure 29b as the one in Figure 29a. This indicates that Equation (18), which is used to estimate the width of the bottom side for interfacial roughness for connected imperfections, is not able to describe the roughness profile when there is the spacing between two imperfections.

The results from the preceding analysis provide a different way to understand the physical implication of tortuosity such that a transitional roughness model is introduced. This transitional model becomes the intermediate between the most simplified continuous roughness model and the generalized model observed from cross-sectional SEM images, Figure 30.

According to the profiles of the metal/oxide interface at various stages of thermal cycling in Figure 31, it is appropriate to consider the most simplified continuous roughness model of Figure 30a to represent the roughness profile at the initial stage of thermal cycling, where small connected saw-like imperfections dominate. It can also be treated as the intermediate section between two large imperfections at a post-failure stage, where similar roughness profiles can be identified as described above.

The transitional roughness model described in Figure 30b is proposed to simulate the roughness at a post-failure stage, Figure 31. The imperfections shown in Figure 30b indicate two large imperfections, as highlighted in the circle in Figure 31, where relatively high-stress levels could be localized somewhere at the bottom of the imperfections. The straight line between two imperfections in Figure 30b represents the small imperfections in the roughness at a post-failure stage in Figure 31, which will not have a large impact on the stress within the large imperfections. It should be noted that in reality, either the distance between two imperfections or the amplitude of roughness could be varied as a function of temperature and number of cycles, Figure 30c. These parameters are taken as their mean values (constant) for the parametric study described below.

Knowing that distance between imperfections is a global factor compared to the geometrical parameters that are used to characterize the geometry of localized imperfections, it is necessary to conduct another parametric study to evaluate the possible effect of the spacing parameter (D) on the stress level, Figure 29. The spacing parameter (D) is incorporated into the FE models, and other factors, such as the size of the imperfection itself (the amplitude and width), are held constant. The parametric study in the current section only deals with the effect of the global parameters on the stress levels at the valley of TC.

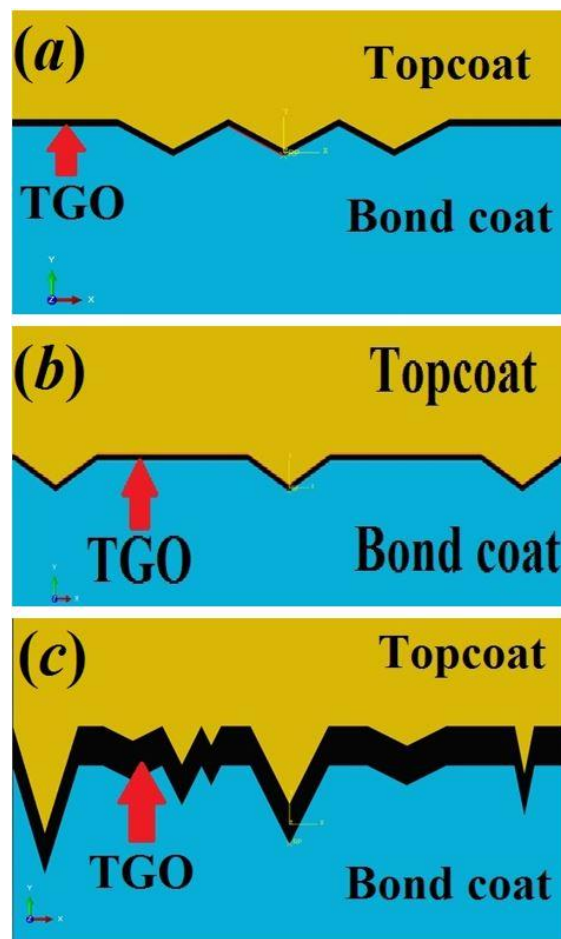


Figure 30. Different models used to describe the interfacial roughness profile: (a) continuous roughness model, (b) transitional roughness model, (c) generalized roughness model.

Accordingly, an equation describing the new width of local imperfections is required when spacing is used in the FE model. The spacing incorporated via the tortuosity becomes:

$$T_L = \frac{2b'N + (N - 1)D}{L_0} \quad (28)$$

where b' is the new length of the hypotenuse of the isosceles-approximated roughness profile after the spacing parameter is included in the FE model. Furthermore, N is the number of imperfections at the interface of the current FE model, D is the spacing parameter and L_0 is the total width of the roughness profile described in the FE model, Figure 29. Based on the definition of an isosceles triangle, the new width of the isosceles in triangular-approximated roughness is defined as:

$$W_L = 2\sqrt{b'^2 - A^2} \quad (29)$$

where W_L defines the local width of the isosceles in triangular-approximated roughness. Substituting Equation (29) into Equation (28), the new width of the isosceles in triangular-approximated roughness with a defined number of imperfections N can be obtained from:

$$W_L = 2\sqrt{\left[\frac{T_L L_0 - (N - 1)D}{2N}\right]^2 - A^2} \quad (30)$$

Equation (30) only works once Equation (28) is satisfied. That is,

$$W_L \times N + (N - 1) \times D = L_0 \quad (31)$$

In other words, the spacing parameter has to be determined once the number of imperfections is defined. The spacing could be obtained by substituting Equation (30) into Equation (31) to yield,

$$D = \frac{L_0^2(T_L^2 - 1) - 4N^2A^2}{2L_0(N - 1)(T_L - 1)} \quad (32)$$

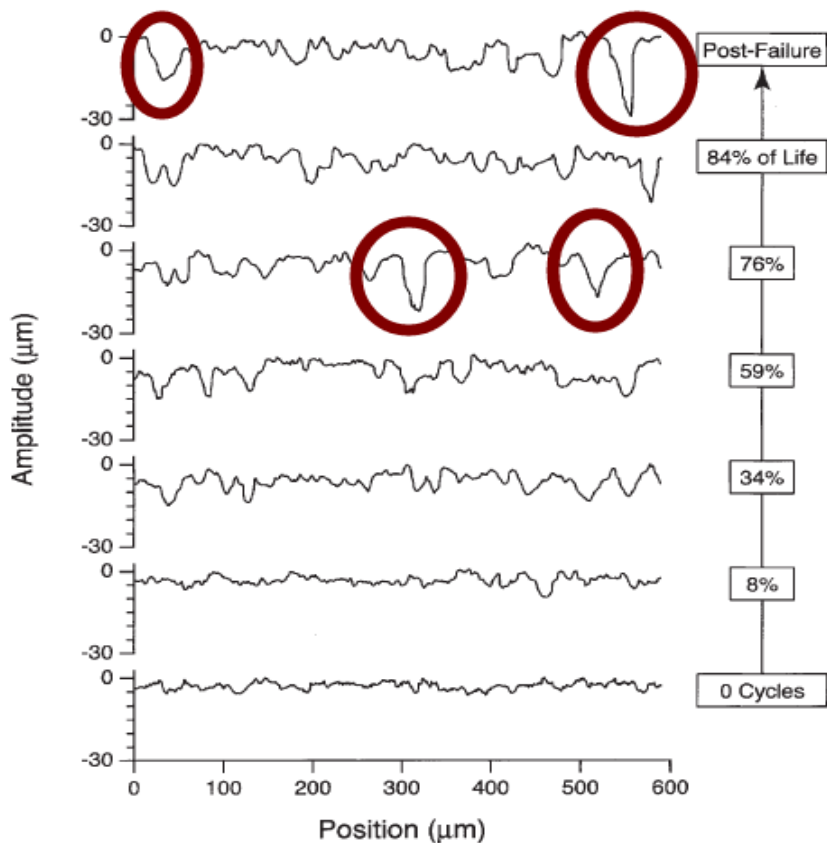


Figure 31. Profiles of the metal/oxide interface extracted from cross-sectional images at various stages of thermal cycling, illustrating the continuous evolution of interface morphology during cyclic exposure.

In this study, the amplitude A and tortuosity T_L of roughness are characterized from a reference group, Table 3, as the transitional roughness model simulates the roughness at a post-failure stage. The total width of the roughness profile L_0 was selected as 300 μm since it is wide enough to incorporate roughness with spacing integrated into the model. The global spacing parameter D and local width W_L of imperfections are described as a function of the number of imperfections in the FE model, Figure 32. It is noted that Equations (30)–(32) are validated, as there is no spacing between imperfections where the maximum width of local imperfections equals approximately 13.76 μm when most imperfections are incorporated into the FE model, Table 3. Importantly, even if the tortuosity and average amplitude are predetermined for a specific number of cycles, it can be seen from Figure 32 that the interfacial roughness profile still needs to be determined from the number of noticeable imperfections N within a defined length of interfacial roughness. Figure 33 illustrates different roughness profiles with the same combination of tortuosity and amplitude but different local widths and spacing parameters. Details are given in Table 4.

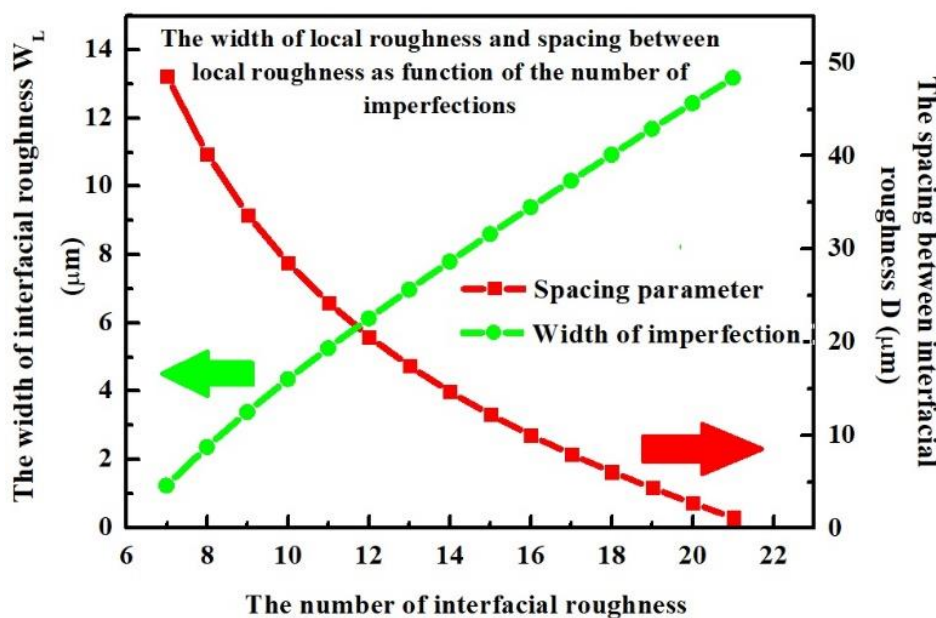


Figure 32. Global spacing parameter D and local width of imperfection W_L as a function of the number of interfacial imperfections.

Table 4. Parameters used in FE analysis in terms of the global spacing parameters.

No# of FE Model	D (μm)	W_L (μm)	No# of Imperfections
a	33.68	3.391	9
b	17.44	6.977	13
c	7.95	10.16	17
d	1.164	13.18	21
For all FE cases			
A (μm)		4.12	
d_{TGO} (μm)		4.92	

In other words, all four roughness profiles illustrated in Figure 33 are possible interfacial roughness profiles for the post-failure stage when the number of noticeable imperfections N is selected based on Figure 32. The results of the maximum cooling stresses within 5000 min calculated from the valley of the TC are plotted in Figure 34.

Combining the observation based on the profiles of metal/oxide interface extracted from cross-sectional images at various stages of thermal cycling in Figure 31, it is expected that at the beginning of thermal cycles (thermal cycles < 1500 cycles), the increasing stress is facilitated for roughness profiles with a wider local length and narrower spacing between neighbouring imperfections that can be treated as a plateau between neighbouring imperfections. Nevertheless, the resulting current stress from different transitional roughness models only indicates the variation of stress level at a post-failure stage of lifetime, since the amplitude and tortuosity parameters used in Equations (30) and (32) are obtained at 177 cycles from cyclic experimental data and fitted into FE models. There exists a potential to describe the geometrical variation for transitional roughness models throughout the life span since the amplitude and tortuosity in Equations (30) and (32) have been recorded as a function of thermal cycles [13]. The challenge is to determine the number of noticeable imperfections N as a function of thermal cycles, Equation (32), and therefore it is difficult to define the spacing D as a function of time.

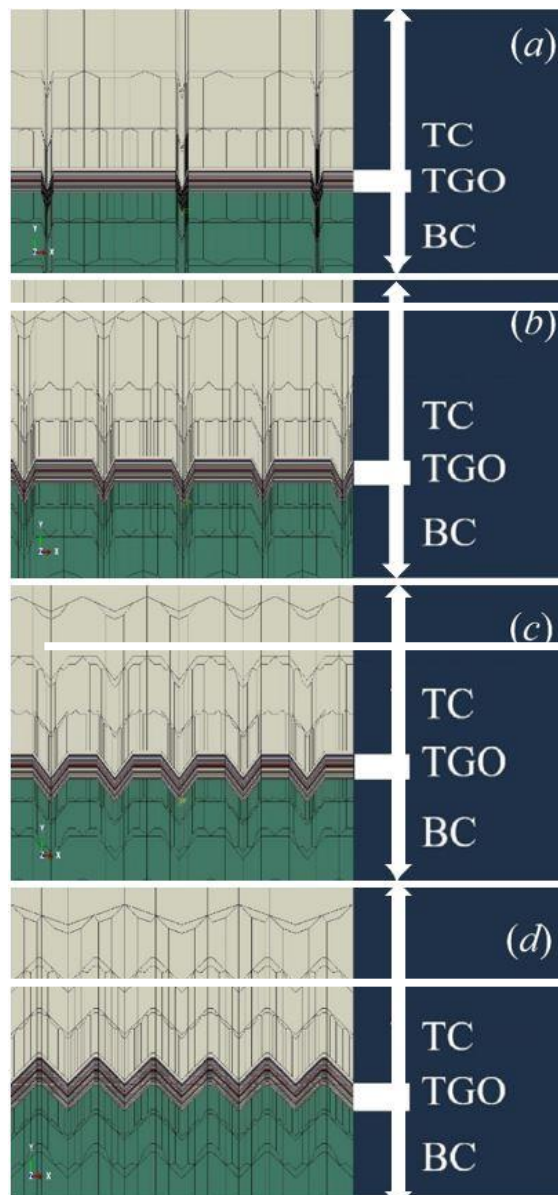


Figure 33. Interfacial roughness profile for different spacing between imperfections. where the interfacial roughness profile (**a-d**) are characterized by parameters provided in Table 4.

However, it was suggested that the roughness level increases as the thermal cycle proceeds [12,13,26]. This indicates that the number of noticeable imperfections N should increase as the time approaches the failure time. Incorporating the trend of increasing N into Equations (30) and (32), it can be qualitatively confirmed that the spacing between neighbouring imperfections decreases and the local width increases as a function of time, which demonstrates that the evolution of interfacial roughness might follow the sequence (a) to (d) in Figure 33.

The stresses described in the preceding sections are the maximum out-of-plane residual stresses upon cooling during thermal cycles. For cases of extreme roughness profile in the current study, e.g., the case (a), the ratio of amplitude over local width is greater than unity. It is not surprising that the black curve has the highest rate of increasing stress among all curves in Figure 34 since it has the narrowest width that boosts the stress concentration. It is also not surprising that there exists a stress inversion as the thermal cycle proceeds. It occurs due to a lack of relatively close neighbouring imperfections, as mentioned in Section 4.1.2. This phenomenon is position-dependent as the current position is located

at approximately 1.27 μm away from the bottom of the TC, Table 3. There is a relatively large variation of stresses as a function of time as the position shifts up or down, towards or away from the interface.

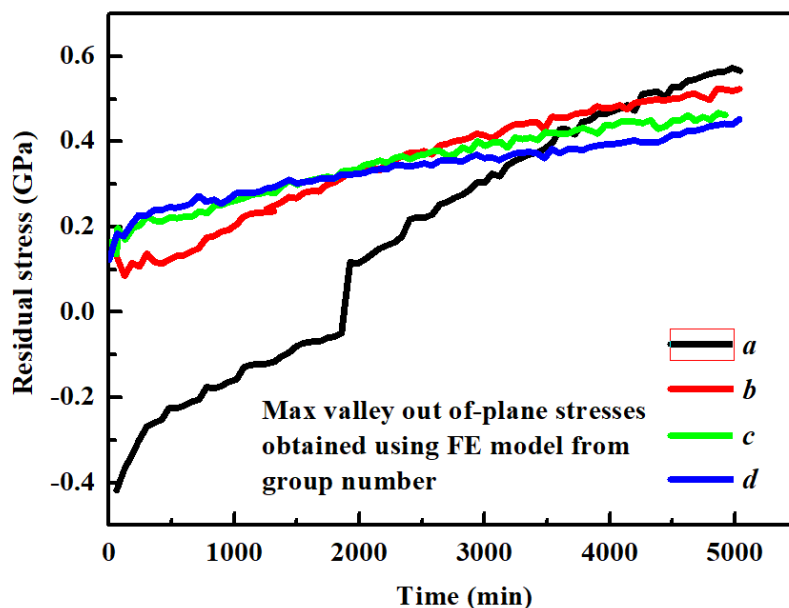


Figure 34. Results of the calculated out-of-plane thermal stresses within the TC with respect to spacing between imperfections.

The introduction of the transitional roughness model gives a proper explanation of the geometrical implication of tortuosity considering global factors. At the same time, it helps the FE model approach the actual cross-section in experimental observation. Theoretically, the experimentally-measured interfacial roughness parameters, characterized by either amplitude, tortuosity or growth of TGO thickness, are statistically mean values within a defined length of interfacial roughness profile during a defined period of the thermal cycle. In reality, the measured value of amplitude, local width for each individual imperfection, as well as spacing between neighbouring imperfections are randomly distributed, as indicated by Figures 30c and 31. To simulate this, a generalized roughness model is established with randomly distributed roughness parameters and integrated into the FE model and shown in Figure 35. For the case of an interface with a randomly distributed roughness profile, the calculated stress becomes more complicated at the valley of the TC, where excessively sharp tip roughness-imperfections are identified.

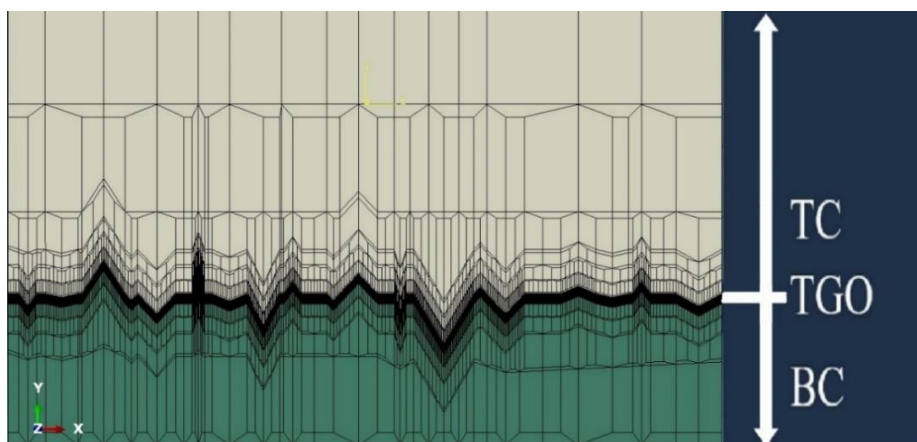


Figure 35. Generalized roughness model using a randomly distributed roughness profile.

4.3. The Effect of Stress Distribution on Positions of Cracks within TC and TGO Layers

As described in the preceding section, the width of the bottom side estimated by Equation (18) fails to characterize the roughness profile when there is spacing between two imperfections. To characterize the interfacial roughness profile at a post-failure stage, a transitional roughness model is proposed where the effect of spacing between imperfections is described by adding parameters into the FE model, Equation (32). Generally speaking, the concept of width of imperfection is redefined as the local width of imperfections W_L , which is no longer limited to the description of the length of the bottom side of the triangular-shaped imperfection, Figure 28. On the other hand, the amplitude measured from experimental data takes the average value according to

$$A = \sqrt{2}RMS = \sqrt{\frac{2}{N} \sum_{i=1}^N y_i^2} \quad (33)$$

The parameters measured experimentally are all average values and provide a general trend as a function of the number of cycles and temperature. In “true” roughness profiles described by the schematic diagram in Figure 30c, the magnitude of amplitude, as well as the width of imperfections, are randomly distributed for individual imperfections. Compared with the true roughness profile from cross-sectional images extracted from the SEM [12], it is possible that the roughness profile model established by using average geometrical parameters from experimental data fails to reflect the “true” roughness profile at the interface where deep, sharp imperfections could possibly exist at the post-failure stage, as indicated by the highlighted circles in Figure 31.

Deep, sharp imperfections simulated using triangular-shaped roughness profiles imply a relatively high ratio of A/W , as illustrated by Figure 28. This will lead to a stress singularity at the valley of the TC close to the interface. In order to examine the effect of sharpness on the stress distribution, imperfections with a high ratio of A/W in the continuous roughness model with 1.5 times amplitude are selected, Figure 20c. Out-of-plane residual stresses are then calculated at different positions away from the valley within the TC. In order to compare the difference of residual stresses at the valley of the TC estimated from the FE model, the positions where stress is calculated are selected close to the ones in Figure 26, where original amplitudes were used in the FE modelling process.

The resulting out-of-plane residual stresses are shown in Figure 36 and are compared with the stresses obtained by using the regular roughness-amplitude FE model, Figure 26.

It is confirmed again that out-of-plane residual stresses are impeded by the excessive increase in amplitude where a relatively large ratio A/W is expected, especially for stresses close to the interface. This can be seen from the difference in stress magnitude at shallow positions of the bottom of the TC, indicated by the black curve in both Figures 26 and 36. A rapid reduction of stress is identified at initial cycles in varying degrees at different positions. However, all curves remain uniformly increasing throughout the entire calculating time. The cyan curve, similar to the preceding section, indicates the residual stresses outside the valley of the TC. Except for the difference in stress level, there is no discrepancy for stress outside the valley compared to those within the valley, with respect to a general trend of increasing stress. There are no significant differences between the two cyan curves in Figures 26 and 36, yet we obtained stress singularity for a large ratio of A/W in the transitional model in Figure 34. Hence, it is strongly suspected that the lack of difference related to the general trend of stresses between the two FE results is due to the excessively close neighbouring imperfections simulated from a continuous roughness model that inhibits the variation of residual stresses, as described in Section 4.1.2.

Stress in the transitional roughness model Figure 33a is determined at different positions away from the valley of the TC and shown in Figure 37. It is obvious that there are large discrepancies between the stresses obtained at different positions compared to the stresses obtained through the continuous roughness model. These discrepancies can be

explained by the smaller interaction on the individual stress level, as there is larger spacing between neighbouring imperfections for the transitional roughness model.

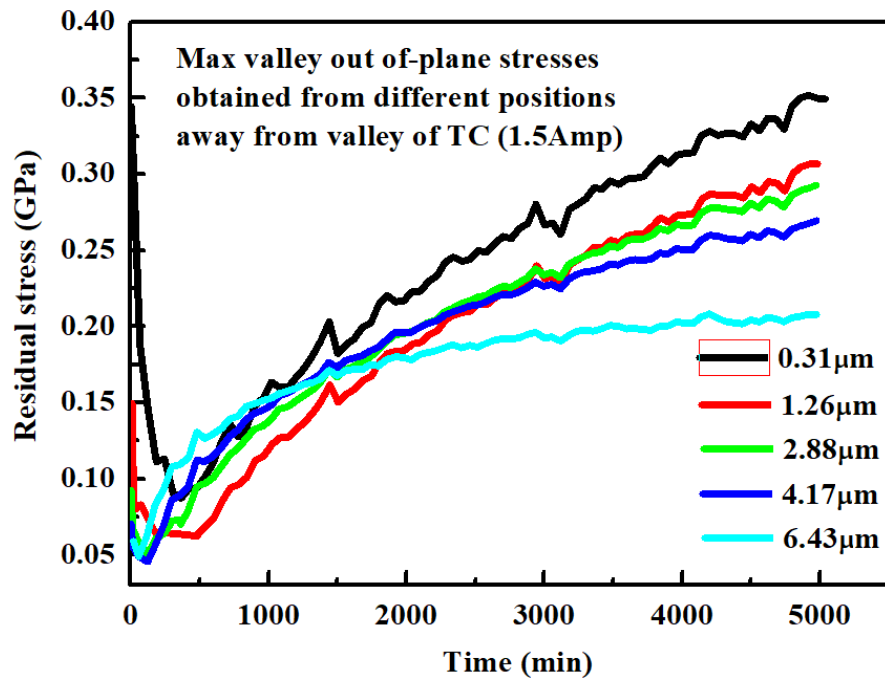


Figure 36. Out-of-plane residual cooling stresses calculated at the valley of TC as a function of time with several selected positions using $1.5\text{ }\mu\text{m}$ roughness amplitude.

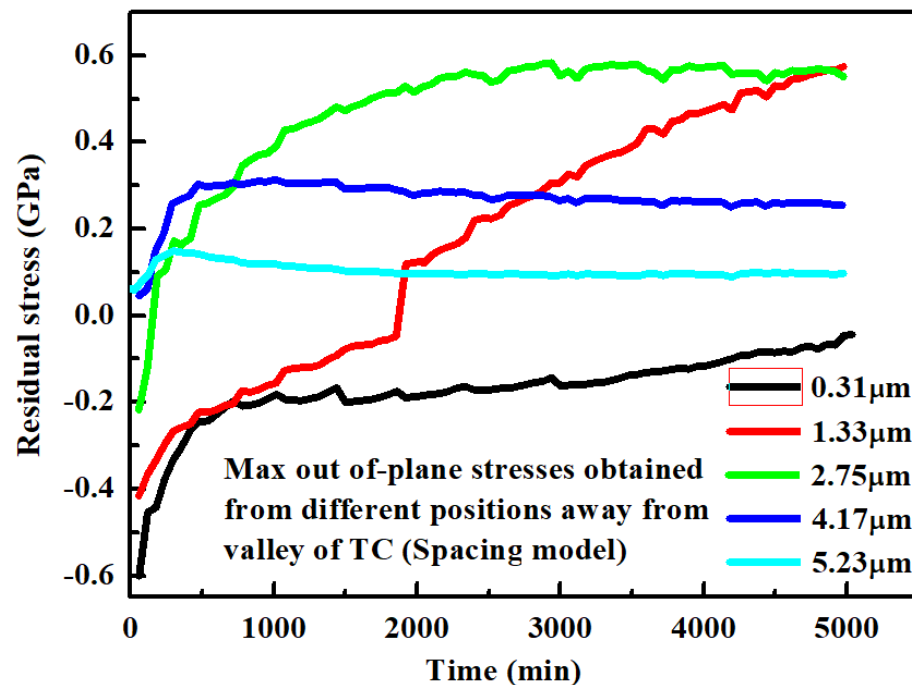


Figure 37. Out-of-plane residual cooling stresses calculated at the valley of the TC as a function of time at several positions using the transitional roughness model.

In contrast to Figure 36, the out-of-plane residual stresses close to the valley of the TC ($0.31\text{ }\mu\text{m}$ away), indicated by the black curve in Figure 37, are in compression within the entire 5000 min thermal cycles. This is considered to impede the nucleation and propagation of cracks parallel to the interface. A rapid stress increase is found for stresses

just a little above the first position, represented by the red and green curves, respectively, accompanied by a stress inversion, which occurs as a function of position and time. With the positions moving into the shallower portion of the TC, there is an obvious decrease in stress level calculated at 4.17 μm and 5.23 μm away from the bottom of the valley in the TC in later thermal cycles. Similar to the analysis in the preceding section, the cyan curve describes the general trend of residual stresses outside the valley of imperfections. Considering the possible positions where the maximum out-of-plane stress occurs, it is reasonable to expect that a crack might develop somewhere around intermediate positions (positions between 1.33 μm and 2.75 μm away from the bottom of the TC as indicated in Figure 37) as the total roughness amplitude is assumed to be about 4.12 μm .

It is observed that the onset of stress inversion varies as a function of position. It could be expected that the red curve, which has the most rapid growth rate, reaches the critical stress level that triggers the initiation of a horizontal crack. However, it is noted that the time for stress inversion for the red curve occurs relatively late in the thermal cycle. This might indicate that the initiation of a horizontal crack as residual stresses reach critical value could be delayed, which is in agreement with experimental observations [11].

According to the stress analysis above, it can be concluded that the onset of residual stress inversion occurs earlier (black-red-green) as the calculated positions move perpendicularly away from the bottom of the TC/TGO interface. This implies that stress at shallower positions might reach the critical level that initiates a horizontal crack at an earlier stage of thermal cycle. However, current FE models are established where residual stresses are calculated without consideration of interfacial roughness evolution as a function of time. We note that the interfacial roughness grows as a function of the thermal cycle, which implies the shortening of spacing between neighbouring imperfections and the widening of local width for individual imperfections. This, in turn, implies that the positions where the possible maximum residual stress occurs could also move close to the bottom of the valley within the TC, as indicated by positions where the maximum stress is identified in Figure 36. Combining the schematic diagram in Figure 38 and failure mechanism summarized in [18], and assuming that the shape of the roughness of an individual imperfection becomes sharper as the thermal cycle proceeds, the stress conditions at the valley of the TC may change.

In order to describe the relationship between positions of maximum stress and possible crack initiation, several stages need to be examined for the entire lifetime with respect to the roughness profile. For Stage “0”, the interfacial roughness at the beginning of the thermal cycle is described in Figure 31 “0 cycles”, where relatively small and uniformly distributed roughness imperfections are identified close to the interface between the TC and the BC, and where the thickness of any pre-existing TGO layer is neglected. The interfacial roughness can be profiled using the continuous roughness model and average roughness amplitude parameters from the initial stage of the thermal cyclic experimental results. The maximum residual stress at stage “0” at the initial thermal cycle can be found close to the valley of the TC, although the magnitude of the residual stress is too small to initiate horizontal crack nucleation.

For stage I, as indicated in Figure 38a, the growth of a few small imperfections could be expected and described as the transitional roughness model with relatively large spacing and short local widths, Figure 33a. Since there is little interaction between neighbouring imperfections, the rapid growth of valley stress could be expected. It is noted that as the increase in amplitude raises the sharpness of the imperfections, it also facilitates the growth of out-of-plane residual stress to a certain degree. There might be an initiation of horizontal cracks somewhere at intermediate positions where stress inversion takes place within a short period of time (Figure 37, positions between the red and green curve). This rapidly increasing stress is balanced by the creep effect of the BC, especially for the area close to the interface where massive stress relaxation takes place during the high temperature holding time. The creep effect is also reflected by the increase of roughness level, where more imperfections are formed due to inelastic deformation as the thermal cycle proceeds.

The resulting shortening of spacing parameter and widening of local width, as well as the growth of roughness amplitude (represented by stage II in Figure 38b and 34% to 76% of life cycles in Figure 31), facilitates interaction between neighbouring imperfections and thus inhibits the growth of residual stresses.

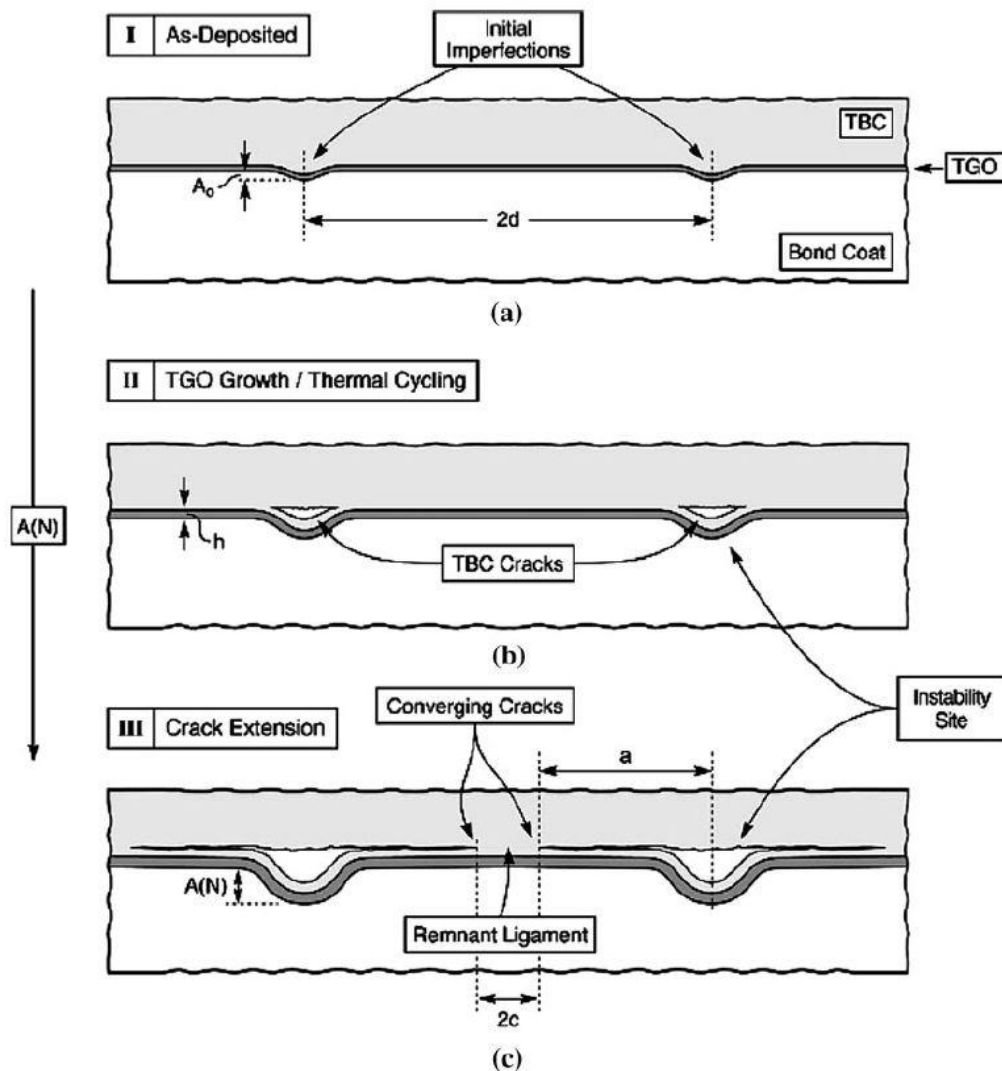


Figure 38. Failure of an EB-PVD TBC system driven by a cyclic instability in the thermally grown oxide layer [18]. (a) Interfacial roughening at stage of as-deposited (b) Crack initiation as TGO growth (c) The propagation of interfacial cracks.

Stage II in Figure 38b can be described in Figure 33b,c for FE mapping. According to the results from the preceding analysis, the positions of the maximum residual stress start to move back to the valley of the TC. Since the horizontal crack propagates already at a relatively shallow position during stage I, the positions of maximum residual stress might shift the possible cracking positions down, or alternatively, might cause the downward extension of the crack accompanied by an expansion of the crack size perpendicular to the interface within the valley of the TC, as indicated in Figure 38c.

As the thermal cycle approaches the post-failure indicated by stage III in Figure 38c, the appropriate FE model is described by either Figure 33d or the continuous roughness model where geometrical roughness parameters are taken from experimental data of the post-failure stage thermal cycle. According to the stress analysis in the preceding section,

the maximum residual stresses are identified at the bottom of the valley within the TC in Figure 26, where the crack is expected to propagate along with the interface.

The generalized roughness model is introduced with a relatively large roughness level at the interface to attempt to profile the randomly distributed peaks and valleys formed at post-failure stages during cyclic thermal simulation, Figure 31. For stress calculated at a shallow valley with low roughness amplitude, the general trend for out-of-plane residual stresses is the same as that obtained in the continuous roughness model, i.e., the residual stress is tensile and decreases as the positions move perpendicularly away from the bottom of the TC. However, for stress at a deep valley with high roughness amplitude, the maximum out-of-plane residual stress has unrealistic values and is concentrated at the tip of the bottom of the valley of the TC, as indicated in Figure 39.

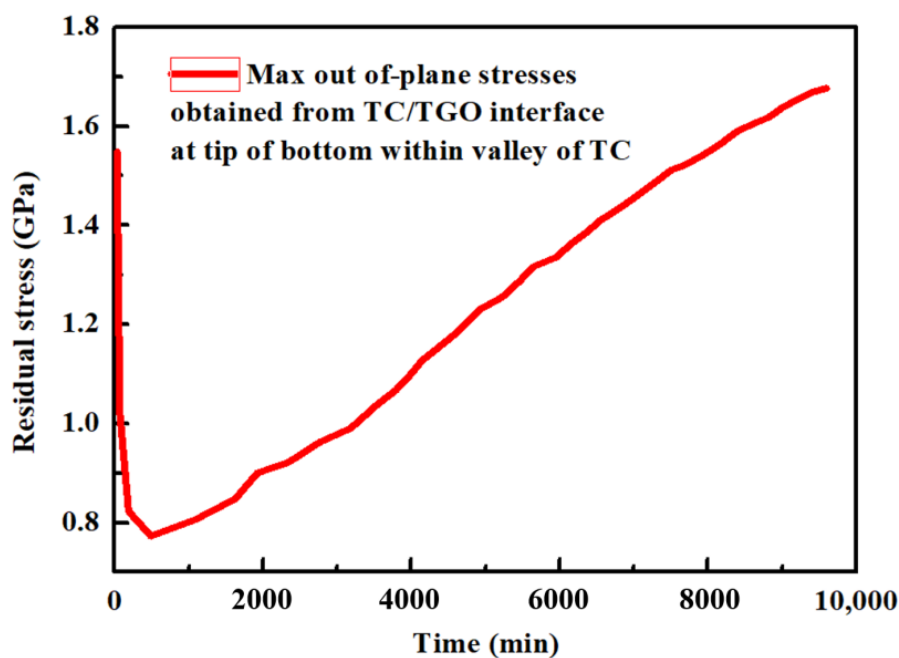


Figure 39. Valley stress at the tip of the bottom at the valley of the TC obtained from the generalized roughness approximated model.

As the results are obtained from the perfect non-cracking FE model, it is reasonable to consider that the magnitude of the stress is large enough to facilitate the crack propagation along the interface between the TC/TGO layer.

It can also be seen that the general trend for residual stresses in Figure 39 is similar to the red curve in Figure 21, where the residual stresses are from closely located imperfections using the continuous roughness model. There also exists a stress singularity within the TGO layer, in particular at imperfections with relatively large roughness. For imperfections with small roughness levels, the variation of residual stress within the TGO layer is illustrated in Figure 40. It shows the stresses at two randomly selected cycles through FE results.

It is concluded that the magnitude of compressive residual stress increases to the maximum level upon cooling and decreases within about 10 min during the reheating period. The overgrowth tensile stress upon the heating process is rapidly relaxed due to the creep effect at high temperatures, resulting in a stress-free state during the holding period. The magnitude of out-of-plane compressive residual stresses within the TGO layer decreases as the thermal cycle proceeds [11,13,26,27]. Specifically, there exists a tensile state for TGO residual stress calculated close to the TC/TGO interface with a relatively large roughness profile, as can be seen in Figure 41.

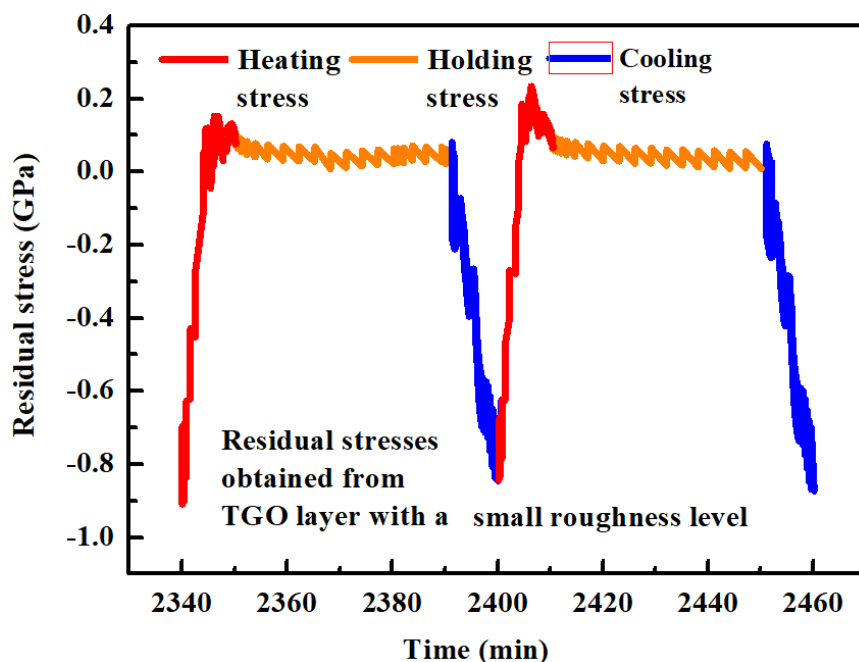


Figure 40. The out-of-plane cyclic residual stress within the TGO layer using a model with small roughness imperfections under cyclic thermal conditions.

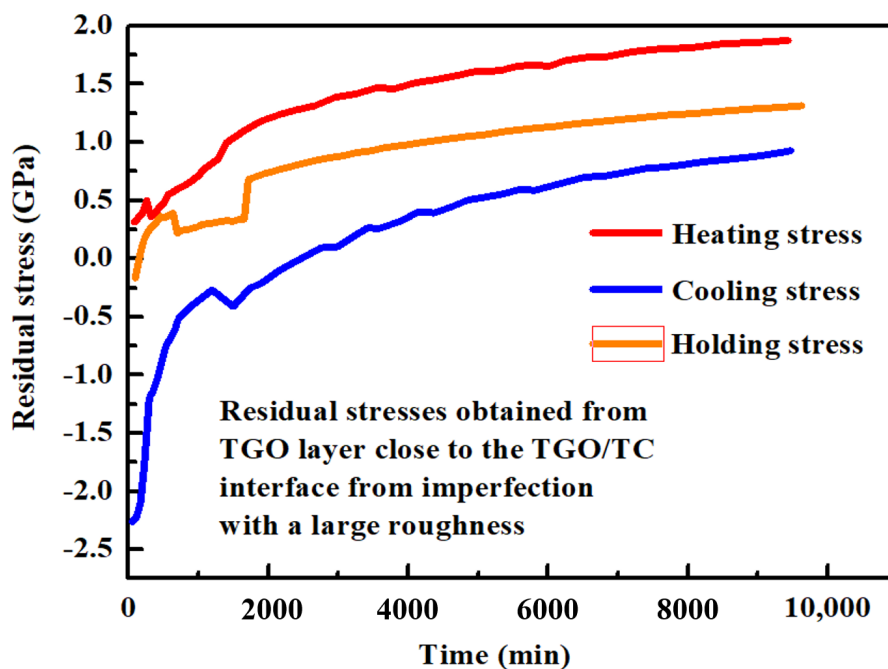


Figure 41. The maximum residual stress calculated within the TGO close to the TC/TGO interface.

It should be noted that the “holding stress” is different from the stress obtained in Figure 40, and increases as a function of thermal cycles. This stable increase of holding stress is a consequence of the geometrical discontinuity at the tip of roughness, where the excessive geometrical sharpness results in significant pressure on the TGO material concentrated in that area. This leads to the failure of stress relaxation. Since stress relaxation is limited during high temperatures, there exists a tensile stress state at the end of the heating process during thermal cycles. This holding stress remains tensile, and its magnitude increases as the thermal cycle proceeds, which leads to a relatively large magnitude of out-of-plane tensile stress at the interface close to the TC/TGO layer. Therefore, it is

plausible to expect that the penetration of the horizontal crack occurs at a valley of the TGO layer close to the TC/TGO interface by the convergence of separated cracks within the TC and BC.

Compared to TGO residual stress close to the TC/TGO interface, the stress near the TGO/BC interface is close to the regular stress state of the TGO layer, Figure 42. The cooling stress shows an initial increase of tensile stress and a rapid decrease until reaching the large magnitude of compressive stress. The initial increase of stress indicates the stress from untransformed metallic BC, and then a rapid decrease suggests the material is undergoing phase transformation. The remaining portion of compressively decreasing out-of-plane stress indicates a typical stress behaviour of fully transformed TGO layer at later thermal cycles, the blue curve in Figure 42 shows the general trend of cooling stress of a TGO layer that undergoes phase transformation from a metallic platinum-modified aluminum layer (Pt-Al) to a predominant alpha-alumina layer [3,27]. Although it has a similar sharp roughness with a high ratio of A/W , it is found that the significant creep behaviour of BC reflected by the large creep prefactor shown in Equation (12) would rapidly relax the stress close to the interface of BC/TGO layer, which explains that the stress singularity calculated within the TGO close to the TC/TGO interface (Figure 41) would be hardly observed within TGO close to the BC/TGO interface (Figure 42).

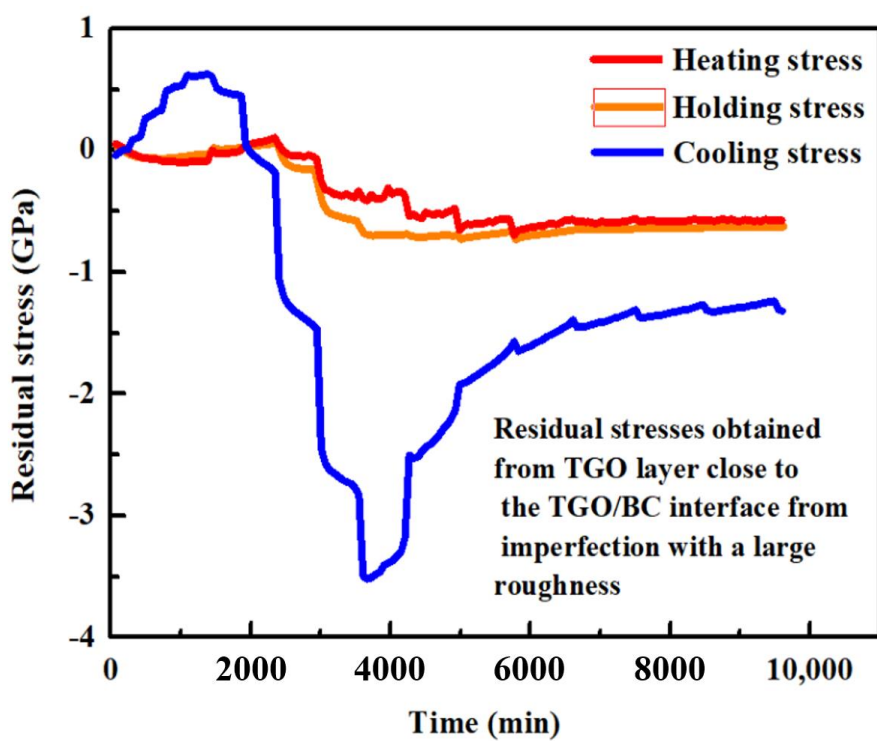


Figure 42. The maximum residual stress calculated within the TGO close to the TGO/BC interface.

5. Conclusions

In this paper, FE models that use temperature-process dependent model parameters were developed, and the out-of-plane residual stresses are calculated for EB-PVD TBCs at maximum cooling point under thermal cyclic conditions. The interfacial roughness was characterized based on cross-sectional images from SEM, where the roughness amplitude and width of the bottom side of imperfections are defined to describe the continuous saw-like interfacial roughness profile. The FE models were implemented by using transversely isotropic elastic properties, and a parametric study was conducted to determine the effect of different roughness levels on stress distributions on different layers. Based on a different way to comprehend the physical implication of tortuosity, a transitional roughness model was developed to characterize the spacing between imperfections with a redefinition of

the local width of triangular-approximated roughness. The transitional roughness model provides a good approximation to simulate roughness between mid-stage to post-failure stages. These developments permit the cracking position to be described as a function of time with the evolution of interfacial roughness and shifting of identified positions of maximum stress. The stress singularities can also be identified at extremely sharp imperfections using either the transitional roughness model or generalized roughness model. Specifically, by calculating stress at different positions within both the TC and TGO layer, the influence of which on possible positions where the crack from different layers coalescence is revealed.

Author Contributions: B.Z.: Conceptualization, Methodology, Validation, Investigation, Writing—original draft. K.C.: Conceptualization, Writing—review and editing, Supervision, Project administration, Resources, Funding acquisition. N.B.: Writing—review and editing, Supervision, Resources, Funding acquisition. All authors have read and agreed to the published version of the manuscript.

Funding: This research was funded by national Research Council Canada, DTS Program, A1-018177.

Institutional Review Board Statement: Not Applicable.

Informed Consent Statement: Not Applicable.

Data Availability Statement: Data will be made available on reasonable request.

Acknowledgments: This research was supported by the Air Defence System Program of the National Research Council Canada (DTS-NRC 2016–2017). This work was also financially supported by the Natural Sciences and Engineering Research Council of Canada under grant number (RGPIN-2016-04190). Thanks is also to J. Hong who proposed the idea of the transitional model in the current study.

Conflicts of Interest: The authors report no declaration of interest.

References

1. Busso, E.P.; Qian, Z.Q. A mechanistic study of microcracking in transversely isotropic ceramic–metal systems. *Acta Mater.* **2006**, *54*, 325–338. [[CrossRef](#)]
2. Balint, D.; Kim, S.-S.; Liu, Y.-F.; Kitazawa, R.; Kagawa, Y.; Evans, A. Anisotropic TGO rumpling in EB-PVD thermal barrier coatings under in-phase thermomechanical loading. *Acta Mater.* **2011**, *59*, 2544–2555. [[CrossRef](#)]
3. Tomimatsu, T.; Zhu, S.; Kagawa, Y. Effect of thermal exposure on stress distribution in TGO layer of EB-PVD TBC. *Acta Mater.* **2003**, *51*, 2397–2405. [[CrossRef](#)]
4. Courcier, C.; Maurel, V.; Rémy, L.; Quilici, S.; Rouzou, I.; Phelippeau, A. Interfacial damage based life model for EB-PVD thermal barrier coating. *Surf. Coat. Technol.* **2011**, *205*, 3763–3773. [[CrossRef](#)]
5. Evans, A.G.; He, M.Y.; Hutchinson, J.W. Mechanics-based scaling laws for the durability of thermal barrier coatings. *Prog. Mater. Sci.* **2001**, *46*, 249–271. [[CrossRef](#)]
6. Zhao, X.; Wang, X.; Xiao, P. Sintering and failure behaviour of EB-PVD thermal barrier coating after isothermal treatment. *Surf. Coat. Technol.* **2006**, *200*, 5946–5955. [[CrossRef](#)]
7. Busso, E.; Qian, Z.; Taylor, M.; Evans, H. The influence of bondcoat and topcoat mechanical properties on stress development in thermal barrier coating systems. *Acta Mater.* **2009**, *57*, 2349–2361. [[CrossRef](#)]
8. Liu, D.; Rinaldi, C.; Flewitt, P.E.J. Effect of substrate curvature on the evolution of microstructure and residual stresses in EBPVD-TBC. *J. Eur. Ceram. Soc.* **2015**, *35*, 2563–2575. [[CrossRef](#)]
9. Mao, W.; Zhou, Y.; Yang, L.; Yu, X. Modeling of residual stresses variation with thermal cycling in thermal barrier coatings. *Mech. Mater.* **2006**, *38*, 1118–1127. [[CrossRef](#)]
10. Ahrens, M.; Vaßen, R.; Stöver, D. Stress distributions in plasma-sprayed thermal barrier coatings as a function of interface roughness and oxide scale thickness. *Surf. Coat. Technol.* **2002**, *161*, 26–35. [[CrossRef](#)]
11. Vaidyanathan, K. Surface geometry and strain energy effects in the failure of a (Ni,Pt)Al/EB-PVD thermal barrier coating. *Acta Mater.* **2004**, *52*, 1107–1115. [[CrossRef](#)]
12. Mumm, D.R.; Evans, A.G.; Spitsberg, I.T. Characterization of a cyclic displacement instability for a thermally grown oxide in a thermal barrier system. *Acta Mater.* **2001**, *49*, 2329–2340. [[CrossRef](#)]
13. Wen, M.; Jordan, E.H.; Gell, M. Effect of temperature on rumpling and thermally grown oxide stress in an EB-PVD thermal barrier coating. *Surf. Coat. Technol.* **2006**, *201*, 3289–3298. [[CrossRef](#)]
14. Busso, E.; Lin, J.; Sakurai, S. A mechanistic study of oxidation-induced degradation in a plasma-sprayed thermal barrier coating system. *Acta Mater.* **2001**, *49*, 1529–1536. [[CrossRef](#)]
15. Cheng, J.; Jordan, E.; Barber, B.; Gell, M. Thermal/residual stress in an electron beam physical vapor deposited thermal barrier coating system. *Acta Mater.* **1998**, *46*, 5839–5850. [[CrossRef](#)]

16. Aschauer, E.; Bartosik, M.; Bolvardi, H.; Arndt, M.; Polcik, P.; Davydok, A.; Krywka, C.; Riedl, H.; Mayrhofer, P. Strain and stress analyses on thermally annealed Ti-Al-N/Mo-Si-B multilayer coatings by synchrotron X-ray diffraction. *Surf. Coat. Technol.* **2019**, *361*, 364–370. [[CrossRef](#)]
17. Abadias, G.; Chason, E.; Keckes, J.; Sebastiani, M.; Thompson, G.B.; Barthel, E.; Doll, G.; Murray, C.; Stoessel, C.H.; Martinu, L. Review Article: Stress in thin films and coatings: Current status, challenges, and prospects. *J. Vac. Sci. Technol. A* **2018**, *36*, 020801. [[CrossRef](#)]
18. Yanar, N.M.; Helminiak, M.; Meier, G.H.; Pettit, F.S. Comparison of the Failures during Cyclic Oxidation of Yttria-Stabilized (7 to 8 Weight Percent) Zirconia Thermal Barrier Coatings Fabricated via Electron Beam Physical Vapor Deposition and Air Plasma Spray. *Met. Mater. Trans. A* **2010**, *42*, 905–921. [[CrossRef](#)]
19. Sánchez-González, E.; Miranda, P.; Meléndez-Martínez, J.J.; Guiberteau, F.; Pajares, A. Temperature dependence of mechanical properties of alumina up to the onset of creep. *J. Eur. Ceram. Soc.* **2007**, *27*, 3345–3349. [[CrossRef](#)]
20. Vaßen, R.; Giesen, S.; Stöver, D. Lifetime of Plasma-Sprayed Thermal Barrier Coatings: Comparison of Numerical and Experimental Results. *J. Therm. Spray Technol.* **2009**, *18*, 835–845. [[CrossRef](#)]
21. Baker, M.; Rösler, J.; Heinze, G. A parametric study of the stress state of thermal barrier coatings Part II: Cooling stresses. *Acta Mater.* **2005**, *53*, 469–476. [[CrossRef](#)]
22. Rösler, J.; Baker, M.; Aufzug, K. A parametric study of the stress state of thermal barrier coatings. *Acta Mater.* **2004**, *52*, 4809–4817. [[CrossRef](#)]
23. ABAQUS; HKS Inc.: Providence, RI, USA, 2019.
24. Curry, N.; Tang, Z.; Markocsan, N.; Nylen, P. Influence of bond coat surface roughness on the structure of axial suspension plasma spray thermal barrier coatings—Thermal and lifetime performance. *Surf. Coat. Technol.* **2015**, *268*, 15–23. [[CrossRef](#)]
25. Clarke, D.; Pompe, W. Critical radius for interface separation of a compressively stressed film from a rough surface. *Acta Mater.* **1999**, *47*, 1749–1756. [[CrossRef](#)]
26. Zhang, B.; Chen, K.; Baddour, N.; Patnaik, P. Failure and life evaluation of EB-PVD thermal barrier coatings using temperature-process-dependent model parameters. *Corros. Sci.* **2019**, *156*, 1–9. [[CrossRef](#)]
27. Xie, L.; Sohn, Y.; Jordan, E.H.; Gell, M. The effect of bond coat grit blasting on the durability and thermally grown oxide stress in an electron beam physical vapor deposited thermal barrier coating. *Surf. Coat. Technol.* **2003**, *176*, 57–66. [[CrossRef](#)]